



NRL/FR/6350--17-10,304

## Biomechanical Modeling of the Human Head

PATRICK BREWICK  
ROBERT SAUNDERS  
AMIT BAGCHI

*Center for Computational Science  
Information Technology Division*

October 3, 2017

DISTRIBUTION STATEMENT A: Approved for public release; distribution is unlimited.

REPORT DOCUMENTATION PAGE				Form Approved OMB No. 0704-0188	
Public reporting burden for this collection of information is estimated to average 1 hour per response, including the time for reviewing instructions, searching existing data sources, gathering and maintaining the data needed, and completing and reviewing this collection of information. Send comments regarding this burden estimate or any other aspect of this collection of information, including suggestions for reducing this burden to Department of Defense, Washington Headquarters Services, Directorate for Information Operations and Reports (0704-0188), 1215 Jefferson Davis Highway, Suite 1204, Arlington, VA 22202-4302. Respondents should be aware that notwithstanding any other provision of law, no person shall be subject to any penalty for failing to comply with a collection of information if it does not display a currently valid OMB control number. <b>PLEASE DO NOT RETURN YOUR FORM TO THE ABOVE ADDRESS.</b>					
1. REPORT DATE (DD-MM-YYYY) 03-10-2017		2. REPORT TYPE Formal Report		3. DATES COVERED (From - To) January 2012 - January 2017	
4. TITLE AND SUBTITLE  Biomechanical Modeling of the Human Head				5a. CONTRACT NUMBER	
				5b. GRANT NUMBER	
				5c. PROGRAM ELEMENT NUMBER	
6. AUTHOR(S)  Patrick Brewick, Robert Saunders, and Amit Bagchi				5d. PROJECT NUMBER	
				5e. TASK NUMBER	
				5f. WORK UNIT NUMBER 63-1B44-A7	
7. PERFORMING ORGANIZATION NAME(S) AND ADDRESS(ES)  Naval Research Laboratory 4555 Overlook Avenue, SW Washington, DC 20375-5320				8. PERFORMING ORGANIZATION REPORT NUMBER  NRL/FR/6350--17-10,304	
9. SPONSORING / MONITORING AGENCY NAME(S) AND ADDRESS(ES)  Office of Naval Research 1 Liberty Center 875 N. Randolph St., Suite 1425 Arlington, VA 22203				10. SPONSOR / MONITOR'S ACRONYM(S)  ONR Code 34	
				11. SPONSOR / MONITOR'S REPORT NUMBER(S)	
12. DISTRIBUTION / AVAILABILITY STATEMENT  DISTRIBUTION STATEMENT A: Approved for public release; distribution is unlimited.					
13. SUPPLEMENTARY NOTES					
14. ABSTRACT  Computational modeling, of both humans and animals, has gained momentum for the investigation of traumatic brain injury. These models require both accurate geometric descriptions and a calibrated constitutive model to predict material behavior. The first step in model calibration involves selecting a model form that captures the available experiment data. Model parameters are estimated for each identified material system via optimization by minimizing the error between model predictions and experimental data. This report details model calibration for all materials identified in models of a human head and porcine head/upper torso. The result is a modeling framework and reference tables for future model developers.					
15. SUBJECT TERMS Biomechanics      Network encryption device      Constitutive modeling      Hyperelastic      Viscoelastic Constrained optimization      Parameter estimation      Model calibration      Computational modeling					
16. SECURITY CLASSIFICATION OF:			17. LIMITATION OF ABSTRACT  Unlimited	18. NUMBER OF PAGES  68	19a. NAME OF RESPONSIBLE PERSON Patrick Brewick
a. REPORT Unclassified	b. ABSTRACT Unclassified	c. THIS PAGE Unclassified			19b. TELEPHONE NUMBER (include area code) 202-767-1466

This page  
intentionally  
left blank

## CONTENTS

EXECUTIVE SUMMARY .....	E-1
1. INTRODUCTION .....	1
2. CONSTITUTIVE MODELING .....	1
2.1 Stress-Strain Relationships .....	4
2.2 Equations of State .....	10
2.3 Model Parameter Estimation .....	12
3. RESULTS AND DISCUSSION .....	16
3.1 Materials Modeled via Equations of State .....	16
3.2 Materials with Parameters Estimated through Optimization .....	18
4. SUMMARY .....	48
ACKNOWLEDGMENTS .....	49
REFERENCES .....	50
APPENDIX A—Material Properties and Model Parameters .....	55

## FIGURES

1	Example stress-strain curve demonstrating how strain energy density is obtained. The shaded area beneath the curve represents the strain energy density for a uniaxial stress .....	2
2	Demonstration of model convergence with decreasing step size for different material models. (Model predictions shown at or approaching maximum strain) .....	14
3	Stress-strain data for the pia mater and dura mater (human subject); experimental data originally presented in [28] .....	19
4	Comparison of stress-strain curves for the falx and tentorium (treated as one material) based on a hyperelastic model and experimental data from [59] .....	20
5	Comparison of stress-strain relationship for experimental data from the cornea [31] and hyperelastic model of the sclera .....	21
6	Comparison of stress-strain relationship in compression for experimental data from auricular cartilage [33] and hyperelastic model of the costal cartilage .....	22
7	Stress-strain data for femoral cortical bone at various strain rates; experimental data originally presented in [62] .....	24
8	Comparison of stress-strain curves produced from scaled experimental data of cortical bone [62] (solid lines) and viscoelastic model of cortical skull bone (dashed lines) .....	26
9	Comparison of stress-strain curves produced by scaled experimental data of cortical bone [62] (solid lines) and viscoelastic model of cancellous skull bone (dashed lines) .....	27
10	Comparison of stress-strain curves produced by scaled experimental data of cortical bone [62] (solid lines) and viscoelastic model of mandible bone (dashed lines) .....	28
11	Grey matter stress-strain data for various strain rates (porcine subject); experimental data originally presented in [66] .....	29
12	Comparison of experimental stress-strain data and hyper-viscoelastic model for grey matter for various strain rates (procine subject); experimental data originally presented in [66] .....	30
13	Model-predicted stress for grey matter over a strain range of [-30%,30%] for a variety of strain rates .....	31
14	White matter stress-strain data for various strain rates (procine subject); experimental data originally presented in [66] .....	32

15	Comparison of experimental stress-strain data and hyper-viscoelastic model for white matter for various strain rates (procine subject); experimental data originally presented in [66].....	33
16	Model-predicted stress for white matter over a strain range of [-30%,30%] for a variety of strain rates.....	34
17	Compressive and tensile stress-strain data for porcine skin at various strain rates; experimental data originally presented in [68] (compression) and [69] (tension) .....	35
18	Comparison of experimental stress-strain data and hyper-viscoelastic model for skin for various strain rates (procine subject); experimental data originally presented in [68] (compression) and [69] (tension) .....	36
19	Model-predicted stress for skin over a strain range of [-30%,30%] for a variety of strain rates	36
20	Tensile stress-strain data for a porcine aortic valve at various strain rates; experimental data originally presented in [70] .....	37
21	Comparison of experimental stress-strain data and hyper-viscoelastic model for the heart for various strain rates (procine subject); experimental data originally presented in [70] .....	38
22	Model-predicted stress for the heart over a strain range of [-30%,30%] for a variety of strain rates .....	39
23	Compressive and tensile stress-strain data for lung tissue (human and porcine) at various strain rates; experimental data originally presented in [42] (tension) and [72] (compression) .	40
24	Comparison of experimental stress-strain data and hyper-viscoelastic model for lung tissue for various strain rates (both human and procine subjects); experimental data originally presented [42] (tension) and [72] (compression) .....	41
25	Model-predicted stress for the lungs over a strain range of [-30%,30%] for a variety of strain rates .....	42
26	Compressive and Tensile stress-strain data for porcine muscle at various strain rates; experimental data originally presented in [73] (compression) and [74] (tension).....	43
27	Comparison of experimental stress-strain data and hyper-viscoelastic model for porcine muscle in tension at various strain rates; experimental data originally presented in [74] .....	44
28	Comparison of experimental stress-strain data and hyper-viscoelastic model for porcine muscle in compressive at various strain rates; experimental data originally presented in [74]..	44
29	Model-predicted stress for muscle tissue over a strain range of [-30%,30%] for a variety of strain rates .....	45
30	Adipose tissue compressive stress-strain data for various strain rates (procine subject); experimental data originally presented in [75] .....	46

31	Comparison of experimental stress-strain data and hyper-viscoelastic model for adipose tissue for various strain rates in compression (procine subject); experimental data originally presented in [75] .....	47
32	Model-predicted stress for adipose tissue over a strain range of [-30%,30%] for a variety of strain rates .....	48

## TABLES

1	Biological Components of the Computational Model of a Head and Torso with Corresponding Constitutive Model and Data Source .....	3
2	Material Parameters for Sample Hyper-Viscoelastic Material .....	15
3	Final Cost Function Values for the Hyperelastic Materials .....	21
4	Parameter Values for the Viscoelastic Model of Cortical Bone .....	25
5	Final Cost Function Values for the Hyper-Viscoelastic Materials .....	48
A1	Material Properties and Model Parameters for Components Modeled via Equations of State...	56
A2	Material Properties and Model Parameters for Components Treated as Hyperelastic Materials	57
A3	Material Properties and Model Parameters for Components Treated as Viscoelastic Materials.	58
A4	Material Properties and Model Parameters for Components Treated as Hyper-viscoelastic Materials .....	59



This page  
intentionally  
left blank

## **EXECUTIVE SUMMARY**

The use of live and computational animal models as surrogates for human testing has gained considerable recent momentum in the investigation of traumatic brain injury. While animal subject testing provides valuable information and data that can also be used for the validation of models, its scope is restricted by ethical concerns, cost, and data with insufficient granularity. Computational models, therefore, act as vital supplementary resources as they reduce these constraints and improve the understanding of blast effects. The creation of computational models requires not only an accurate geometric description but also a calibrated constitutive model to predict material behavior.

This report details the process involved in generating a calibrated constitutive model. First, a constitutive model form that can sufficiently capture the phenomena that occur in the experimental data is chosen based on the latest available literature for each material identified in the geometric model. The constitutive model forms chosen are then detailed and reduced to a functional form compatible with the available experimental data. An optimization scheme is then detailed with the purpose of estimating the constitutive model parameters by minimizing the error between the model predictions and the experimental data set. This process is repeated for each material system identified in the geometric models of a human head and the head and upper torso of a pig. The result is a modular methodology for future model developers to reference.

This page  
intentionally  
left blank

# BIOMECHANICAL MODELING OF THE HUMAN HEAD

## 1. INTRODUCTION

A 2008 RAND report estimates that nearly 20 percent of deployed service members experience some level of traumatic brain injury (TBI) with as much as 70 percent of those injuries coming from blast, which is the primary cause of mild TBI (mTBI) [1]. The exact injury mechanisms in mTBI are not well understood and for obvious reasons the blast events cannot be replicated *in vivo* on human subjects. Thus, in order to better understand mTBI, researchers must rely upon computational simulations [2–9]. Live animal models, e.g., pigs, are also now being used as surrogates to study TBI in humans [10–13]. Due to ethical considerations, cost, and insufficient granularity of data, live animal testing is also being complemented and supplemented by computational modeling [14, 15]. The development of these computational and mathematical models, however, is fraught with issues [16]. One such problem is the determination of appropriate constitutive models and parameters. Many biological materials exhibit large strain and time-dependent anisotropic elasticity with a hysteretic unloading behavior and tension-compression asymmetry. Obviously, to capture this behavior numerically would require an incredibly complex constitutive model. While some researchers have developed highly complex models to capture many of the observed behaviors, these models require a prohibitively large number of parameters not easily obtained [17, 18].

This report seeks to determine and calibrate an appropriate constitutive model for each component of computational models of a human head and the upper torso and head of a pig. These computational models contain all major differentiable components from high resolution computed tomography (CT) and magnetic resonance imaging (MRI) scans. The mechanical difference between components in the human and pig is small [19] and as such they need not be calibrated separately. The remainder of the report is structured into three primary sections. First, a description of the modeling approach and calibration technique is given, which details constitutive model selection and parameter estimation methodology. Next, the parameters values selected for each component in the computational models are discussed. Finally, a summary and conclusions are provided. In addition, there is an appendix with tables summarizing the chosen models and final parameters; this table is intended to assist future researchers and reduce the time required to develop new computational models.

## 2. CONSTITUTIVE MODELING

When quantifying the mechanical properties of a given material, whether structural or biological, it is most convenient to start with the assumption that, at a minimum, stress-strain data is available. The generation of stress on a body is due to the work done by surface or body forces. This work is stored inside the body in the form of strain energy,  $U$ , given by

$$U = \int_V w \, dV \quad (1)$$

where  $W$  is the strain energy density (strain energy per unit volume) and  $V$  represents the volume of the system. The strain energy density is directly related to stress and strain as it constitutes the area under a given stress-strain curve, which can be visualized by Fig. 1. This relation is expressed more generally by Eq. (2) as

$$W = \int \boldsymbol{\sigma} : d\boldsymbol{\epsilon} \quad (2)$$

where  $\boldsymbol{\sigma}$  and  $\boldsymbol{\epsilon}$  are the stress and strain tensors, respectively. The strain energy density function is ideal for material characterization because it can be generalized to capture any stress-strain curve or available experimental data set. This flexibility in modeling stress-strain relations also makes strain energy density highly useful for materials with more challenging properties, such as those found in the human body. The

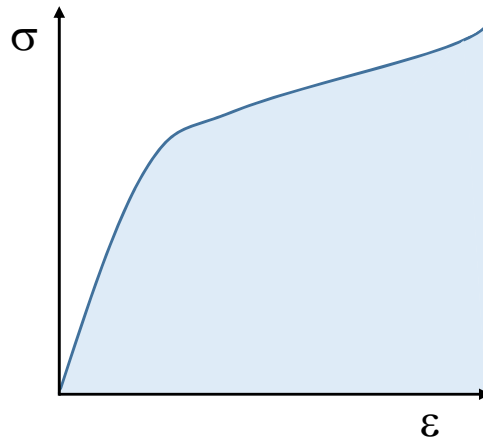


Fig. 1: Example stress-strain curve demonstrating how strain energy density is obtained. The shaded area beneath the curve represents the strain energy density for a uniaxial stress

human body possesses myriad components that can be readily seen in any anatomy textbook or atlas. In practice, the identification of these components depends on the available resolution of images taken with CT and/or MRI scans. Once identified, the different components may be digitally segmented, i.e., differentiated within each image, for use in a computational model [20, 21]. Each of the identified components requires a constitutive model whose parameters must be further identified and calibrated based on experimental data. Accumulating the data needed to calibrate such a large number of constitutive models is a tremendous task, especially for a single research group; thus, it is most beneficial to take advantage of published studies in the available literature. Table 1 presents a summary of the segmented biological components for a model of the human body along with the constitutive model forms considered to best represent each material and the experimental data sources used for model parameter calibration.

Table 1: Biological Components of the Computational Model of a Head and Torso with Corresponding Constitutive Model and Data Source

Component	Constitutive Model	Source
Sinus - Frontal	Equation of State	<sup>a</sup>
Sinus - Maxillary		
Airway		
Cerebrospinal Fluid (CSF)	Equation of State\Hyperelastic	[22, 23]
Ventricles - Lateral		
Ventricles - Third		
Ventricles - Fourth		
Ventricles - Aqueduct of Sylvius		
Ventricles - Foramen of Monro		
Venous Sinuses and Bridging Veins		
Eyes (Vitreous)	Equation of State\Hyperelastic	[22, 24]
Venous Sinus and Bridging Vein Walls	Anisotropic Hyperelastic	[25, 26]
Pia Mater	Hyperelastic	[27, 28]
Dura Mater	Hyperelastic	[28, 29]
Falx Cerebri	Hyperelastic	[30]
Tentorium Cerebella	Hyperelastic	[30]
Sclera and Cornea	Hyperelastic	[28, 31]
Intervertebral Discs	Hyperelastic	[32]
Costal Cartilage	Hyperelastic	[8, 33]
Skull - Cortical	Transversely Isotropic Viscoelastic	[34]
Skull - Cancellous	Transversely Isotropic Viscoelastic	[35, 36] <sup>b</sup>
Mandible	Transversely Isotropic Viscoelastic	[37]
Vertebrae	Viscoelastic	[32] <sup>c</sup>
Ribs	Viscoelastic	[34, 38]
Sternum	Viscoelastic	[32] <sup>c</sup>
Cerebrum - Grey Matter	Hyper-viscoelastic	[8]
Cerebellum - Grey Matter		
Cerebrum - White Matter	Hyper-viscoelastic	[8]
Cerebellum - White Matter		
Brain Stem - Medulla		
Brain Stem - Midbrain		
Brain Stem - Pons		
Spinal Cord		
Optic Nerves		
Skin	Hyper-viscoelastic	[8, 39]
Heart	Hyper-viscoelastic	[8, 40] <sup>d</sup>
Lungs	Hyper-viscoelastic	[41, 42]
Muscles	Hyper-viscoelastic	[8, 40] <sup>d</sup>
Soft Tissue (Aidpose)	Hyper-viscoelastic	[8, 39]

<sup>a</sup> The familiar properties for air at 37 °C and ambient pressure of 1 atm were used.

<sup>b</sup> Values from [36] not taken directly but scaled based on available data.

<sup>c</sup> Values from [32] not taken directly but scaled based on available data.

<sup>d</sup> Values from [40] not taken directly but scaled based on available data.

*Note:* Components grouped with a brace } share parameters for their respective constitutive model.

With proper constitutive models forms chosen based on experimental evidence, it is beneficial to derive the stress-strain relationship for each of the forms presented. The derivation for each model begins from the strain energy density of Eq. (2). Note, in cases where an equation of state was used, the derivation does not begin from the strain energy function as it is not relevant to those material systems. Also note that each derivation will only be shown for a uniaxial case. The procedure to derive a three-dimensional stress state is the same, but those derivations are omitted here for simplicity and brevity.

## 2.1 Stress-Strain Relationships

First, the simplest case of a purely elastic material is derived to demonstrate the method by which the remaining materials are derived. Using the familiar strain-displacement relations and Hooke's law for elastic materials,  $W$  can be expressed as

$$W = \int E \epsilon d\epsilon = \frac{1}{2} E \epsilon^2, \quad (3)$$

where  $\epsilon$  is the axial strain and  $E$  is the elastic or Young's modulus. For more complex material systems that exhibit large non-linear deformations, it is most convenient to formulate the constitutive model in terms of the strain energy density rather than using a Hooke's law approach. The axial stress,  $\sigma$ , can be obtained by taking the derivative of  $W$  with respect to  $\epsilon$ , giving the familiar constitutive relationship for an elastic material as

$$\sigma = \frac{dW}{d\epsilon} = E\epsilon. \quad (4)$$

### 2.1.1 Viscoelastic

For materials exhibiting a linear time dependent viscoelastic behavior, the stress is related to velocity and can be represented by

$$\boldsymbol{\sigma}(t) = \int_0^t d\boldsymbol{\sigma}(t) = \int_0^t \mathbf{C}(t-\tau) \frac{d}{d\tau} \boldsymbol{\epsilon}(\tau) d\tau, \quad (5)$$

where  $\mathbf{C}(t)$  is a time-dependent elastic modulus tensor. This time-dependent tensor may be expanded as

$$\mathbf{C}(t) = \mathbf{C}_s g(t) \quad (6)$$

where  $\mathbf{C}_s$  is the canonical elastic modulus tensor for an isotropic, linear elastic solid [43] and  $g(t)$  is some relaxation modulus. A generalized Maxwell model is commonly used to define the relaxation modulus [44]; the Maxwell model is represented by a Prony series of  $M$  terms as

$$g(t) = 1 - \sum_{j=1}^M g_j \left(1 - \exp^{-t/\tau_j}\right), \quad (7)$$

where  $g_j$  is a normalized modulus and  $\tau_j$  is a material time constant. Using Eq. (6) the stress may then be rewritten as

$$\boldsymbol{\sigma}(t) = \int_0^t g(t-\tau) \mathbf{C}_s \frac{d}{d\tau} \boldsymbol{\epsilon}(\tau) d\tau = \int_0^t g(t-\tau) \frac{d}{d\tau} (\mathbf{C}_s \boldsymbol{\epsilon}(\tau)) d\tau. \quad (8)$$

Note that the second modification may be made since  $\mathbf{C}_s$  is a constant matrix; while it might seem counter-intuitive to place this matrix inside the derivative operator, it is convenient to have the matrix product  $\mathbf{C}_s \boldsymbol{\varepsilon}$ .

Under the assumption of a uniaxial stress state for an isotropic homogeneous material, the shear strains within  $\boldsymbol{\varepsilon}$  are set to zero and, through the use of Hooke's law, the remaining strains share the relation  $\varepsilon_{22} = \varepsilon_{33} = -\nu \varepsilon_{11}$ ,  $\nu$  is Poisson's ratio. These simplifications with respect to strain produce a stress vector with a single non-zero entry, just as the uniaxial name would imply; thus the matrix product  $\mathbf{C}_s \boldsymbol{\varepsilon}$  can be reduced to a single non-zero component  $\sigma_{11}$  written in terms of the only independent strain  $\varepsilon_{11}$

$$\sigma_{11}(t) = \int_0^t g(t-\tau) \frac{d}{d\tau} \left[ \frac{E}{(1+\nu)(1-2\nu)} ((1-\nu) - 2\nu^2) \varepsilon_{11} \right] d\tau. \quad (9)$$

Several simplifications may be made by canceling out the terms in the numerator and denominator and substituting the full expression for the relaxation modulus in Eq. (7), producing

$$\sigma_{11}(t) = \int_0^t E \left[ 1 - \sum_{j=1}^M g_j \left( 1 - \exp^{-(t-\tau)/\tau_j} \right) \right] \frac{d}{d\tau} (\varepsilon_{11}) d\tau. \quad (10)$$

Assuming a linear relationship between strain and strain rate such that  $\varepsilon_{11}(\tau) = \dot{\varepsilon} \tau$  and  $\frac{d}{d\tau} (\varepsilon_{11}) = \dot{\varepsilon}$  yields

$$\sigma(t) = \int_0^t E \dot{\varepsilon} \left[ 1 - \sum_{j=1}^M g_j \left( 1 - \exp^{-(t-\tau)/\tau_j} \right) \right] d\tau. \quad (11)$$

In the final equation, the required constitutive model parameters are the elastic modulus,  $E$ , the non-dimensional moduli,  $g_j$ , and the material time constants,  $\tau_j$ . Note that  $g_j$  is restricted such that  $\sum_{j=1}^M g_j \leq 1$ .

### 2.1.2 Hyperelastic

There are a number of hyperelastic constitutive models available to describe a material exhibiting large strain elasticity. For the case of biological materials, which are generally incompressible or nearly incompressible, the constitutive model forms are limited to those that are derived to model rubber-like nearly incompressible materials. The most common forms of hyperelastic models derived for this purpose are the Ogden model and the variants of the generalized polynomial model. As mentioned previously, a material exhibiting a hyperelastic-type behavior is generally easier to represent by directly forming a strain energy potential; thus, this potential is the starting point of the proceeding derivations.

#### Ogden Model

Starting with the Ogden model [45] produces

$$W = \sum_{i=1}^N \frac{2\mu_i}{\alpha_i^2} \left( \bar{\lambda}_1^{\alpha_i} + \bar{\lambda}_2^{\alpha_i} + \bar{\lambda}_3^{\alpha_i} - 3 \right) + \sum_{i=1}^N \frac{1}{D_i} \left( J^{el} - 1 \right)^{2i}, \quad (12)$$



where  $N$  controls the order of the Ogden model and  $\bar{\lambda}_j = J^{-\frac{1}{3}} \lambda_j$  with  $\lambda_j$  being the principal stretches and  $J$  the total volume ratio defined as  $J = \lambda_1 \lambda_2 \lambda_3$ . The total volume ratio is related to the elastic volume ratio  $J^{el}$  from Eq. (12) as

$$J^{el} = \frac{J}{J^{th}} \quad (13)$$

where  $J^{th}$  represents the volumetric deformation due to thermal expansion; in the absence of thermal expansion,  $J^{el}$  simply reduces to  $J^{el} = J$ . The parameters  $\mu_i$ ,  $\alpha_i$ , and  $D_i$  are related to material properties. Specifically  $\mu_i$  is related to the initial shear modulus  $G_0$  by

$$G_0 = \sum_{i=1}^N \mu_i. \quad (14)$$

The parameter  $D_1$  is related to the initial bulk modulus  $K_0$  as

$$K_0 = \frac{2}{D_1}. \quad (15)$$

There is also an important relationship between the initial shear modulus and bulk modulus of a material and its Poisson's ratio. The Poisson's ratio may be computed according to the following relation

$$\nu = \frac{3K_0/G_0 - 2}{6K_0/G_0 + 2} \quad (16)$$

where this expression is often used as a means of assessing compressibility. Equation (12) may be simplified by assuming that the material is completely (or nearly) incompressible, thus  $J = 1$  and the strain energy density becomes

$$W = \sum_{i=1}^N \frac{2\mu_i}{\alpha_i^2} (\lambda_1^{\alpha_i} + \lambda_2^{\alpha_i} + \lambda_3^{\alpha_i} - 3). \quad (17)$$

For the incompressible material under an axial stress state, the principal stretches are related by  $\lambda_2 = \lambda_3 = \lambda_1^{-1/2}$ , and this allows the strain energy density to be simplified to

$$W = \sum_{i=1}^N \frac{2\mu_i}{\alpha_i^2} (\lambda_1^{\alpha_i} + 2\lambda_1^{-\alpha_i/2} - 3). \quad (18)$$

The uniaxial stress,  $\sigma$ , can be easily determined to be

$$\sigma(\lambda_1) = \frac{dW}{d\lambda_1} = \sum_{i=1}^N \frac{2\mu_i}{\alpha_i} (\lambda_1^{\alpha_i-1} - \lambda_1^{-\alpha_i/2-1}). \quad (19)$$

The required constitutive model parameters for the uniaxial Ogden model are the moduli,  $\mu_i$ , and material constants,  $\alpha_i$ . In this model, the selection of  $\mu_i$  must follow the constraint,  $\sum_{i=1}^N \mu_i > 0$ . This constraint ensures that the initial modulus,  $\mu_0 = \sum_{i=1}^N \mu_i$ , is always positive.

### Generalized Polynomial Model

The generalized polynomial model, when operating under an assumption of material incompressibility, begins from

$$W = \sum_{i+j=1}^N C_{ij} (\bar{I}_1 - 1)^i (\bar{I}_2 - 1)^j, \quad (20)$$

where  $\bar{I}_i$  are the deviatoric strain invariants defined by  $\bar{I}_1 = \bar{\lambda}_1^2 + \bar{\lambda}_2^2 + \bar{\lambda}_3^2$  and  $\bar{I}_2 = \bar{\lambda}_1^{-2} + \bar{\lambda}_2^{-2} + \bar{\lambda}_3^{-2}$ . Following the same procedure as before with respect to the principal stretches yields

$$W = \sum_{i+j=1}^N C_{ij} (\lambda_1^2 + 2\lambda_1^{-1} - 1)^i (\lambda_1^{-2} + 2\lambda_1 - 1)^j. \quad (21)$$

From which the uniaxial stress can be obtained as

$$\begin{aligned} \sigma(\lambda_1) = \sum_{i+j=1}^N C_{ij} \left[ i (\lambda_1^2 + 2\lambda_1^{-1} - 1)^{i-1} (2\lambda_1 - 2\lambda_1^{-2}) (\lambda_1^{-2} + 2\lambda_1 - 1)^j \right. \\ \left. + j (\lambda_1^{-2} + 2\lambda_1 - 1)^{j-1} (2 - 2\lambda_1^{-3}) (\lambda_1^2 + 2\lambda_1^{-1} - 1)^i \right]. \quad (22) \end{aligned}$$

Only the modulus term,  $C_{ij}$  is needed for the polynomial model. Generally values of  $N > 2$  are not used due to the number of required calibration parameters. The initial modulus,  $\mu_0$ , is obtained by  $2(C_{10} + C_{01})$ . Similar to the Ogden model, the polynomial model is subject to the constraint,  $\sum_{i+j=1}^N C_{ij} > 0$ , to ensure the modulus is always positive.

### Special Cases

From the Ogden model and generalized polynomial model, a few useful special cases of hyperelastic models can be derived.

*Reduced Polynomial Model* — The first special case is the reduced polynomial model, which is the same as the polynomial model with  $j = 0$ . The reduced polynomial models is given by

$$W = \sum_{i=1}^N C_{i0} (\lambda_1^2 + 2\lambda_1^{-1} - 1)^i, \quad (23)$$

with uniaxial stress obtained as

$$\sigma(\lambda_1) = \sum_{i=1}^N C_{i0} \left[ i (\lambda_1^2 + 2\lambda_1^{-1} - 1)^{i-1} (2\lambda_1 - 2\lambda_1^{-2}) \right]. \quad (24)$$

*Yeoh Model* — A further reduction of the reduced polynomial model is the Yeoh model [46]. The Yeoh model simply restricts the reduced polynomial model to have  $i = 1, 2, 3$ ; which results in

$$W = C_{10} (\lambda_1^2 + 2\lambda_1^{-1} - 1) + C_{20} (\lambda_1^2 + 2\lambda_1^{-1} - 1)^2 + C_{30} (\lambda_1^2 + 2\lambda_1^{-1} - 1)^3, \quad (25)$$

with uniaxial stress obtained as

$$\sigma(\lambda_1) = (2\lambda_1 - 2\lambda_1^{-2}) \left[ C_{10} + 2C_{20} (\lambda_1^2 + 2\lambda_1^{-1} - 1) + 3C_{30} (\lambda_1^2 + 2\lambda_1^{-1} - 1)^2 \right]. \quad (26)$$

*Neo-Hookean Model* — In the next instance, the neo-Hookean model can be derived through a special case of either the Ogden model or the polynomial model. Using  $i = 1$  in both models and letting  $\alpha = 2$  or  $j = 0$  in the Ogden or polynomial models, respectively, the neo-Hookean model can be obtained as

$$W = C_{10} (\lambda_1^2 + 2\lambda_1^{-1} - 1), \quad (27)$$

with uniaxial stress given by

$$\sigma(\lambda_1) = C_{10} (2\lambda_1 - 2\lambda_1^{-2}). \quad (28)$$

*Mooney-Rivlin Model* — A final model, the Mooney-Rivlin model, is derived in a similar fashion to the neo-Hookean model. From the Ogden model, the combination of  $\alpha_1 = 2$  and  $\alpha_2 = -2$  can be used; from the polynomial model, the combination of  $i, j = 1, 0$  and  $i, j = 0, 1$  can be used. In either instance, the Mooney-Rivlin model can be obtained as

$$W = C_{10} (\lambda_1^2 + 2\lambda_1^{-1} - 1) + C_{01} (\lambda_1^{-2} + 2\lambda_1 - 1). \quad (29)$$

From which the uniaxial stress can be obtained as

$$\sigma(\lambda_1) = C_{10} (2\lambda_1 - 2\lambda_1^{-2}) + C_{01} (2 - 2\lambda_1^{-3}). \quad (30)$$

### Anisotropic Hyperelastic

Materials that are tube-like in nature, such as fibers or fiber-reinforced structures, are often modeled with cylindrical geometry and anisotropic properties. For this study, the walls of the bridging veins within the brain are treated as a fibrous material and, thus, described with an anisotropic hyperelastic model. Specifically, the walls of the bridging veins are modeled using a constitutive form developed for arterial wall mechanics [26, 47], sometimes referred to as the Holzapfel-Gasser-Ogden model. The corresponding strain energy density function for this constitutive model form is given in Eq. (31)

$$W = \frac{c}{2} (\bar{I}_1 - 3) + \frac{k_1}{2k_2} \left\{ \exp \left[ k_2 (\kappa \bar{I}_1 + (1 - 3\kappa) \bar{I}_4 - 1)^2 \right] - 1 \right\} \quad (31)$$

where  $c$ ,  $k_1$ , and  $k_2$  are material-specific stiffness, stress, and dimensionless parameters, respectively. As a general note, the first term in Eq. (31) acts as an isotropic matrix-type contribution, while the second term represents the anisotropic fiber-type term. The parameter  $\kappa$  controls the degree of anisotropy by characterizing the dispersion of the fibers, and  $\bar{I}_4$  is another deviatoric strain invariant. As defined in [26], the  $\kappa$  term ranges from 0 (anisotropic) to 1/3 (isotropic). More clarification on this parameter may be found in [26];

specifically, an interested reader is directed to Section 4.1 in [26]. As mentioned previously, it is convenient to consider the orientation of fibrous materials in cylindrical coordinates  $(r, \theta, z)$ ; within this coordinate system, the invariants  $\bar{I}_1$  and  $\bar{I}_4$  may be defined as

$$\bar{I}_1 = \lambda_z^2 + \lambda_\theta^2 + (\lambda_z \lambda_\theta)^{-2} \quad (32a)$$

$$\bar{I}_4 = \lambda_z^2 \sin^2 \gamma + \lambda_\theta^2 \cos^2 \gamma \quad (32b)$$

where  $\gamma$  defines the angle between the circumference of the vein wall and the mean orientation of the fiber families comprising the vein walls. The derivation of the uniaxial stress for this model is omitted here because of its complexity; more information about this constitutive model may be found in [26].

### 2.1.3 Hyper-viscoelastic

The final model derivation presented in this study is for materials exhibiting both linear rate dependence and large strain elasticity. For these materials, a hyper-viscoelastic material model is derived from the Ogden model with Prony series viscoelasticity. (The process for incorporating any of the previously shown hyperelastic models with Prony series viscoelasticity is the same as for incorporating Ogden hyperelasticity and, therefore, is omitted for brevity.) Beginning with the strain energy density of Eq. (18), the Boltzmann superposition principle is applied to obtain a time integral as

$$W = \int_0^t \left[ \sum_{i=1}^N \frac{2}{\alpha_i^2} \mu_i(t-\tau) \frac{d}{d\tau} \left( \lambda_1^{\alpha_i} + 2\lambda_1^{-\alpha_i/2} - 3 \right) \right] d\tau. \quad (33)$$

Note that for the polynomial model, or any model derived from the polynomial model,  $C_{ij}$  would become  $C_{ij}(t-\tau)$ . The Prony series may then be incorporated to obtain

$$W = \int_0^t \left\{ \sum_{i=1}^N \frac{2}{\alpha_i^2} \mu_i \left[ 1 - \sum_{j=1}^M g_j \left( 1 - e^{-(t-\tau)/\tau_j} \right) \right] \frac{d}{d\tau} \left( \lambda_1^{\alpha_i} + 2\lambda_1^{-\alpha_i/2} - 3 \right) \right\} d\tau. \quad (34)$$

As before the uniaxial stress is given by  $\sigma = \frac{dW}{d\lambda_1}$ , thus

$$\sigma = \int_0^t \left\{ \sum_{i=1}^N \frac{2}{\alpha_i^2} \mu_i \left[ 1 - \sum_{j=1}^M g_j \left( 1 - e^{-(t-\tau)/\tau_j} \right) \right] \frac{d}{d\tau} \left[ \frac{d}{d\lambda_1} \left( \lambda_1^{\alpha_i} + 2\lambda_1^{-\alpha_i/2} - 3 \right) \right] \right\} d\tau, \quad (35)$$

which may be further simplified to

$$\sigma = \int_0^t \left\{ \sum_{i=1}^N \frac{2}{\alpha_i^2} \mu_i \left[ 1 - \sum_{j=1}^M g_j \left( 1 - e^{-(t-\tau)/\tau_j} \right) \right] \frac{d}{d\tau} \left[ \alpha_i \left( \lambda_1^{(\alpha_i-1)} - \lambda_1^{(-\alpha_i/2-1)} \right) \right] \right\} d\tau. \quad (36)$$

The formulation for nonlinear viscoelastic constitutive models provided in [44] suggests deriving the stress according to

$$\sigma(t) = \int_{-\infty}^t g(t-s) \frac{d}{ds} \left( \frac{\partial W}{\partial \lambda_1} \right) ds. \quad (37)$$

It can be easily shown that substituting the Prony series for  $g(t-s)$  and using the Ogden model for strain energy density (thus inserting Eq. (19) for  $\frac{\partial W}{\partial \lambda_1}$ ), Eq. (37) becomes

$$\sigma(t) = \int_{-\infty}^t \left\{ \left[ g_0 - \sum_{j=1}^M \bar{g}_j \left( 1 - e^{-(t-s)/\tau_j} \right) \right] \frac{d}{ds} \left[ \sum_{i=1}^N \frac{2\bar{\mu}_i}{\alpha_i} \left( \lambda_1^{(\alpha_i-1)} - \lambda_1^{(-\alpha_i/2-1)} \right) \right] \right\} ds, \quad (38)$$

which may be easily re-arranged to match Eq. (36). The only other consideration that must be taken into account is how Eqs. (36) and (38) treat the initial modulus constant,  $g_0$ . Equation (36) is already normalized by  $g_0$  such that

$$\mu_i = \bar{\mu}_i g_0 \quad (39a)$$

$$g_j = \frac{\bar{g}_j}{g_0} \quad (39b)$$

which then allows for the computation of the initial shear modulus as

$$\sum_{i=1}^N \mu_i = \sum_{i=1}^N \bar{\mu}_i g_0 = g_0 \sum_{i=1}^N \bar{\mu}_i = G_0. \quad (40)$$

With this understanding, it may be shown that Eqs. (36) and (38) are perfectly equivalent.

If it may be further assumed that the strain rate is constant, and, thus, the relationship between stretch  $\lambda_1$  and stretch rate  $\dot{\lambda}$  is linear, then the relation  $\lambda_1 = 1 + \dot{\lambda} \tau$  may be substituted into Eq. (36). The stress may again be simplified to

$$\sigma(t) = \int_0^t \left\{ \sum_{i=1}^N \frac{2\dot{\lambda}\mu_i}{\alpha_i} \left[ 1 - \sum_{j=1}^M g_j \left( 1 - e^{-(t-\tau)/\tau_j} \right) \right] \left[ (\alpha_i - 1)(1 + \dot{\lambda}\tau)^{(\alpha_i-2)} + \left( \frac{\alpha_i}{2} + 1 \right) (1 + \dot{\lambda}\tau)^{(-\alpha_i/2-2)} \right] \right\} d\tau. \quad (41)$$

This stress derivation has the same parameters and constraints as both the viscoelastic model and Ogden hyperelastic model previously presented.

## 2.2 Equations of State

For fluids or fluid-like materials, equations of state were used to model the volumetric response of the material.

### 2.2.1 Ideal Gas

The familiar ideal gas equation of state is given by

$$P = \rho R(T - T^Z) - p_a, \quad (42)$$

where  $P$  is pressure,  $R$  is the specific gas constant,  $T$  is the temperature and  $T^Z$  is absolute zero on the temperature scale,  $\rho$  is the density, and  $p_a$  is the ambient pressure.

### 2.2.2 Mie-Grüneisen

The Mie-Grüneisen equation of state is commonly employed for describing underwater shock and is given by

$$P = \Gamma \rho (E_m - E_H) + p_H, \quad (43)$$

where  $E_m$  and  $E_H$  represent the internal and Hugoniot energy per unit mass,  $p_H$  is the Hugoniot pressure, and  $\Gamma$  is the Grüneisen ratio, which is defined as

$$\Gamma = \Gamma_0 \frac{\rho_0}{\rho}, \quad (44)$$

where  $\Gamma_0$  is a material constant and  $\rho_0$  is the reference density. The Hugoniot pressure can be related to its energy term by

$$E_H = \frac{p_H \eta}{2\rho_0}, \quad (45)$$

where  $\eta$  represents the nominal volumetric compressive strain, expressed as  $\eta = 1 - \rho_0/\rho$ . Substituting the relations in Eqs. (44) and (45) into Eq. (43) yields

$$P = p_H \left( 1 - \frac{\Gamma_0 \eta}{2} \right) + \Gamma_0 \rho_0 E_m. \quad (46)$$

Assuming a linear relationship exists between shock velocity  $U_s$  and particle velocity  $U_p$ , those velocities can be related by the expression

$$U_s = c_0 + sU_p, \quad (47)$$

where  $c_0$  is the intercept and  $s$  is the slope of the  $U_s$ - $U_p$  curve. More significantly, though,  $c_0$  represents the bulk speed of sound, i.e., the shock velocity at an infinitesimally small particle velocity, which is defined by

$$c_0 = \sqrt{\frac{K_0}{\rho_0}}. \quad (48)$$

Values for  $s$  may be found in tables of past experiments or by performing a linear regression on shock and particle velocity data. When the shock and particle velocities share a linear relationship, such as the one described by Eq. (47), the Hugoniot pressure may be expressed as

$$p_H = \frac{\rho_0 c_0^2 \eta}{(1 - s\eta)^2}. \quad (49)$$

It is important to note that the  $U_s$ - $U_p$  relationship is sometimes expressed as a cubic polynomial, but this study only considers the linear relationship. Inserting the Hugoniot pressure from Eq. (49) into Eq. (46) yields

$$P(E_m) = \frac{\rho_0 c_0^2 \eta}{(1 - s\eta)^2} \left( 1 - \frac{\Gamma_0 \eta}{2} \right) + \Gamma_0 \rho_0 E_m \quad (50)$$

which is commonly referred to as the “ $U_s-U_p$ ” equation of state. Also, it is important to note that the quantity  $\rho_0 c_0^2$  is equivalent to the bulk modulus at small strains (see Eq. (48)).

### 2.3 Model Parameter Estimation

The parameter values for the various material models were estimated through a few different means. For the fluid or fluid-like biomaterials best modeled using equations of state, the appropriate parameter values were found using standard values for the fluid in question, e.g., air, or values reported in literature, e.g., CSF. For the elastic-type materials, the model parameter values were estimated using optimization.

#### 2.3.1 Optimization Scheme

For the model parameters estimated via optimization, the chosen optimization algorithm was the “global search,” which is an effective algorithm for finding the global minimum in the presence of several local minima. Specifically, this study used the `GlobalSearch` function from MATLAB’s Global Optimization Toolbox [48]. This function uses a large set of trial points to fully explore the parameter space and then employs gradient-based optimization algorithms, e.g., steepest descent, that use the different trial points as starting points. From these trial points, the global search algorithm seeks to identify several basins of attraction, where a basin of attraction represents the set of initial values for the parameter vector that converge to the same local minimum. By employing many trial points and attempting to identify several basins of attraction, the global search method efficiently seeks out the global minimum. It should be noted the general approach for material parameter estimation lends heavily from the methods described in [49].

#### 2.3.2 Cost Function

The cost or objective function  $O$  for the optimization was based on minimizing the residual between the data and the model predictions, as shown by Eq. (51)

$$O = \sqrt{\sum_k^{N_m} [\hat{\sigma}(\epsilon_k) - \sigma(\epsilon_k)]^2} \quad (51)$$

where  $\hat{\sigma}(\epsilon_k)$  and  $\sigma(\epsilon_k)$  are the model-predicted and experimental stress values, respectively, at the  $N_m$  discretely measured strains  $\epsilon_k$ . It is often convenient to normalize the cost function in order to keep its evaluation in a range spanning zero to unity (although values larger than unity are possible); thus Eq. (52) was developed by normalizing Eq. (51) by the measured stress.

$$\bar{O} = \frac{O}{\sqrt{\sum_k^{N_m} \sigma^2(\epsilon_k)}} \quad (52)$$

In some cases, more than one stress-strain data set was available. In these cases, Eq. (52) was evaluated for each data set and then the cost function became the summation across all evaluations of Eq. (52). This is shown for an arbitrary material with  $N_d$  data sets in Eq. (53).

$$\bar{O} = \bar{O}_1 + \bar{O}_2 + \cdots + \bar{O}_{N_d} = \sum_{m=1}^{N_d} \bar{O}_m \quad (53)$$

One potential issue with Eq. (53) is that assumes all data sets are of equal value and, thus, deserving of equal weight. This assumption may be modified through the use of a weight vector  $\mathbf{w}$  that contains individual weights  $w_i$  for each of the  $N_d$  data sets, as shown in Eq. (54). Constructing the cost function in this manner allows a user maximum control in steering the optimization process.

$$\bar{O} = w_1 \bar{O}_1 + w_2 \bar{O}_2 + \cdots + w_{N_d} \bar{O}_{N_d} = \sum_{m=1}^{N_d} w_m \bar{O}_m \quad (54)$$

### Gathering Experimental Data

The experimental data needed for calibrating the material models were collected from previously published studies in the literature. Specifically, data from figures in those studies were carefully extracted via computer vision techniques and graphical methods. The extracted data was conditioned and regularized, if necessary, before being treated as the experimental data in the optimization scheme, i.e., the experimental stress in Eq. (51). The inherent variability among published studies meant that some data sets were originally presented as a discrete set in their respective figures whereas others were continuous plots; however, both of these data sets became discrete by virtue of the data harvesting methodology employed herein. In order to compensate for this effect, the optimization operated on a data set of 20 equally-spaced interpolated stress-strain points regardless of the size or format of the original extracted data vector. However, for transparency with regard to the originally extracted data, the figures in this study that display the results of the optimization show the discrete extracted data points; these are treated as the “experimental data” in those figures.

#### 2.3.3 Constraints

The model predictions for  $\hat{\sigma}(\epsilon_k)$  were based on the different models for the various materials. Equations (11), (19), and (41) were used for the viscoelastic, hyperelastic, and hyper-viscoelastic materials, respectively. Each equation has its own set of parameters and those parameters were assigned various constraints, making the optimization problem a constrained optimization. The specific constraints are discussed with their material type below.

#### Hyperelastic

The hyperelastic materials were considered the most straightforward case for parameter estimation because, unlike models with viscoelastic terms, the model equation for the hyperelastic materials did not involve numerical integration. The global search algorithm was used to find the optimal parameters for Eq. (19) with the added constraint that parameters  $\mu_i$  must follow  $\sum_{i=1}^N \mu_i > 0$  (similarly,  $\sum_{i+j=1}^N C_{ij} > 0$ ). Another important constraint was placed on the model itself to ensure that the stress and strain followed Drucker’s first stability criterion [50] given by

$$d\sigma : d\epsilon \geq 0 \quad (55)$$

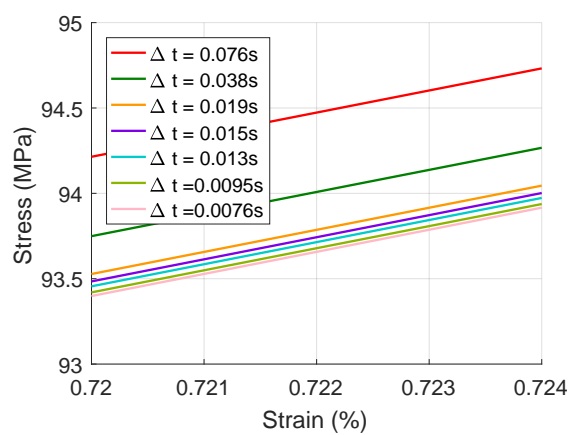
where  $d\sigma$  is the stress increment tensor and  $d\epsilon$  is the strain increment tensor.



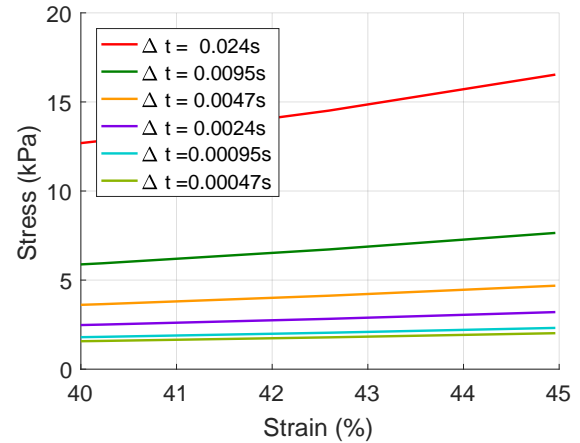
## Viscoelastic

In terms of constraints for the viscoelastic materials, there were several important considerations. Each shear (relaxation) modulus ratio  $g_j$  had to fall within the interval (0,1) and obey the inequality  $1 - \sum_{j=1}^M g_j \geq 0$ . Additionally, the time constants were constrained to always be positive, i.e.,  $\tau_j > 0$ . Another important consideration was that the computation of the stress for the viscoelastic model involves numerical integration (Eq. (11)), which meant that the integration time step  $\Delta t$  had to be carefully chosen. This issue of time step size mostly pertained to the data from tests with slower strain rates, i.e.,  $\dot{\epsilon} < 1/s$ .

For instance, the experimental data for cortical bone, which is presented in Section 3.2.2, achieved roughly the same maximum strain at six different strain rates ranging from  $1 \times 10^{-3}/s$  to  $1.5 \times 10^3/s$ . That maximum strain, which was around 0.72 percent, would be achieved in approximately  $4.8 \times 10^{-6}$  s for the highest strain rate but would require 7.2 s for the lowest. Thus, discretizing these two time domains with the same number of increments would yield two vastly different time step sizes. Given that the time step sizes for the highest strain rate would be extremely small by default, only a few increments are needed; however, using an equivalent number of increments for the lowest strain rate would result in a time step size of insufficient resolution. Ultimately, an appropriate time step size may be chosen by studying how the model predictions converge with decreasing time step size, as demonstrated by Fig. 2a. For the model of the cortical bone the relative deviation in model predictions across the time step sizes was only around 1 percent, but Fig. 2b shows that for a model of grey matter with a similarly slow strain rate ( $1 \times 10^{-2}/s$ ) the relative deviation was much more significant, at over 700 percent. (Note that the time steps in Fig. 2b are smaller than those in Fig. 2a.) By studying the convergence behavior of the different constitutive model forms, appropriate time step sizes were chosen for each material exhibiting viscoelastic properties to ensure sufficient accuracy in the model predictions.



(a) Model for cortical bone at strain rate of  $1 \times 10^{-3}/s$



(b) Model for grey matter at strain rate of  $1 \times 10^{-2}/s$

Fig. 2: Demonstration of model convergence with decreasing step size for different material models. (Model predictions shown at or approaching maximum strain)

### Hyper-viscoelastic

The hyper-viscoelastic materials were estimated in the same manner as the hyperelastic and viscoelastic materials. The same constraints were placed on the viscoelastic parameters of the Prony series and on the  $\mu_i$  terms for the hyperelastic component of the model. Due to the hyperelasticity, compliance with Drucker's first stability criterion was also included as a constraint for these models. Several of the materials possessed data sets at multiple strain rates, meaning that weighting vectors were also necessary. In addition to these constraints, the hyper-viscoelastic materials also included another consideration for parameter uniqueness.

One of the more persistent challenges in parameter estimation and optimization involves uniqueness. Specifically, the ability to identify a unique set of optimal parameters. While this challenge was encountered for both the hyperelastic and viscoelastic materials, it was found that the hyper-viscoelastic materials posed the most significant issues related to uniqueness. For instance, performing optimization on the hyperelastic or viscoelastic materials would result in different optimal parameters for each trial, but the normalized prediction error was similar each time and the variation in the optimal parameters was limited. In contrast, the normalized error for the hyper-viscoelastic materials could differ by an order of magnitude between two trials with accompanying optimal parameter vectors that are vastly different.

In order to better illustrate this phenomenon, a sample material was created using arbitrary values for the hyperelastic and viscoelastic parameters, which are given in Table 2. Using these material parameters, stress-strain curves were created for six strain rates spanning from 0.01/s to 1000/s by decade, i.e., power of 10; the applied strains were compressive. The stress-strain information was then used as the experimental data for the global search optimization; this data set is referred to as "pseudo-data" for the purposes of this study. The advantage of using known material parameters and pseudo-data is obvious in that, since the ground truth values are known, the results of the optimization may be much more precisely assessed.

Table 2: Material Parameters for Sample Hyper-Viscoelastic Material

Component	Ogden terms			Prony series			$\bar{O}$
	$\mu_i$	$\alpha_i$		$g_j$	$\tau_j$		
True Value	$i = 1$	$1.00 \times 10^5$	3.00	$j = 1$	0.08	$1.00 \times 10^1$	
	$i = 2$	$-5.00 \times 10^4$	1.00	$j = 2$	0.25	$1.00 \times 10^{-3}$	
Trial 1	$i = 1$	$-1.46 \times 10^5$	0.50	$j = 1$	0.22	$8.22 \times 10^{-2}$	0.6064
	$i = 2$	$2.75 \times 10^5$	3.05	$j = 2$	0.66	$2.29 \times 10^{-9}$	
Trial 2	$i = 1$	$7.14 \times 10^5$	3.70	$j = 1$	$6.36 \times 10^{-4}$	$8.10 \times 10^{-3}$	0.1142
	$i = 2$	$8.63 \times 10^6$	3.76	$j = 2$	0.99	$1.01 \times 10^{-7}$	

The results of two different trials of global search optimization are presented in Table 2 with the randomly-generated initial parameter vector being the only difference between the two trials. The estimates for the Ogden terms for Trial 1 are reasonable reflections of their true values, especially for the  $\alpha$  terms (although their  $i$  indices are swapped). In contrast, the Ogden terms from Trial 2 are universally too

large, with the  $\mu$  terms lacking a negative value and both  $\alpha$  values being greater than their true values. Neither trial experienced any notable success in estimating the Prony terms. Paradoxically, however, Trial 2 boasts a normalized prediction error over five times smaller than that for Trial 1.

While it is acknowledged that this study omits necessary discussions on parameter identifiability and sensitivity, the broader point about challenges in unique parameter identification still holds. Despite the apparent evidence to the contrary, Trial 2 provided the closest fit to the original data set even though none of its individual parameter estimates were closest to their true values. This example is meant to serve as an illustration of these parameter estimation challenges and an aid in interpreting the results presented for the hyper-viscoelastic biomaterials included in the model.

### 3. RESULTS AND DISCUSSION

The identification of the model parameters for the various components of the finite element (FE) model are detailed below. Many of the soft biological materials were treated as nearly incompressible and, therefore, were given a Poisson's ratio of  $\nu = 0.499999$ . In addition, these soft biomaterials were also given a bulk modulus of 2.19 GPa [8] unless otherwise noted. Tabulated summaries of the relevant material properties and estimated parameter values are provided in Appendix A.

#### 3.1 Materials Modeled via Equations of State

A brief summary of the fluid-like materials described by an equation of state and included in the model is given below.

##### 3.1.1 Sinuses and Airway

The sinuses in the head model were treated as air and, therefore, were modeled using the ideal gas equation of state. It is assumed that the ambient pressure  $p_a$  is 1 atm, which is equivalent to 101.325 kPa. The density of air at 1 atm and 35 °C, which is close to body temperature of 37 °C, is 1.1455 kg/m<sup>3</sup>. The specific gas constant  $R$  for air is 287.058 J/(kg·°K); since a Kelvin temperature scale is being employed,  $T^Z$  may simply be taken as 0. Lastly, the air must be given a viscosity to satisfy ABAQUS's requirement for shear properties — at 37 °C the viscosity of air is  $19.2 \times 10^{-6}$  Pa·s. These values are listed in Table A1 without a specific source because the properties of air are widely agreed upon.

The airway was modeled with the ideal gas equation of state using the same parameters as for the air-filled sinuses.

##### 3.1.2 Cerebrospinal Fluid (CSF), Ventricles, and Venous Sinuses and Bridging Veins

The ventricles of the brain are cavities filled with cerebrospinal fluid (CSF). This fluid component of the brain was modeled using the  $U_s-U_p$  equation of state. The CSF was treated as an incompressible fluid whose density was provided by [23] (see Table A1). For the purposes of FE modeling, CSF is often given the same bulk properties as water ( $K_0 = 2.19$  GPa) [9, 51]. The venous sinuses and bridging veins primarily concern the fluid inside, namely blood. For the purposes of this study, the blood was modeled the same as CSF and water; given the minor role of these components in the greater model, this assumption had little impact.

The determination of the parameters  $c_0$ ,  $s$ , and  $\Gamma_0$  necessary for the  $U_s-U_p$  equation of state, commonly referred to as the shock Hugoniot parameters, is more difficult as the field of biomechanics currently lacks specific experimental studies on shock Hugoniot parameters for CSF. However, given the congruity in material properties between water and CSF, this dearth of reliable data may be compensated for by using shock Hugoniot data for water. While a variety of shock Hugoniot parameters exist for water, as may be seen in [52], there tends to be agreement on the bulk speed of sound for water as  $c_0 = 1480$  m/s [22, 52–54]. Additionally, the parameter  $s$  is generally agreed to fall within the interval 1.75–1.79 [22, 52, 54]; this study uses  $s = 1.79$ . However, there is less agreement for the Grüneisen parameter  $\Gamma_0$ . Both [22] and [54] use  $\Gamma_0 = 1.65$ , but [52] reports using  $\Gamma_0 = 0.4934$ ; this study adopts  $\Gamma_0 = 1.65$ .

In addition to the shock Hugoniot parameters, the CSF was also given a viscosity, where the viscosity was based on the Newtonian model shown in Eq. (56)

$$\tau = \zeta \dot{\gamma} \quad (56)$$

where  $\tau$  is the equivalent shear stress,  $\zeta$  is the viscosity, and  $\dot{\gamma}$  is the engineering shear strain rate. At the average human body temperature (37 °C) the viscosity of water is 0.6913 mPa·s [55]. Despite its many similarities to water, the presence of CSF could potentially impact its viscosity. However, experiments performed by [56] revealed that CSF has a viscosity of 0.7–1.0 mPa·s at 37 °C, very nearly the same as water. Therefore, this study adopts a viscosity of 0.7 mPa·s for CSF.

Since these materials are so close to incompressible, an equation of state may not be necessary for modeling the volumetric component. An equivalent incompressible model can be used to better predict the shear behavior. Thus, the CSF can also be modeled as a hyperelastic material governed by a neo-Hookean model, as in Eq. (27). Using the shear modulus of 22.53 kPa provided in [8],  $C_{10}$  becomes 11.27 kPa. Additionally, utilizing the generic bulk modulus for soft materials yields  $D_1 = 9.13 \times 10^{-1}$  GPa<sup>-1</sup>.

### 3.1.3 Vitreous – Eyes

When modeling the eyes, the majority of the eye structure was treated as the fluid-like vitreous humour. This was another component modeled using the  $U_s-U_p$  equation of state. The necessary material properties for the eyes, given in Table A1, are provided by [24]. While [24] does not provide the shock Hugoniot data, the bulk speed of sound may be computed using the bulk modulus for vitreous (2000 MPa) and its density, yielding  $c_0 = 1450$  m/s. Given that the bulk properties of the vitreous are similar to those of water, it is assumed that the shock Hugoniot parameters  $s$  and  $\Gamma_0$  for water may also be used for the vitreous. This is an admittedly bold assumption, but shock Hugoniot data is not readily available for the vast majority of biological materials.

Like the CSF, the vitreous may also be modeled as a neo-Hookean material. The value for  $D_1$  may be quickly computed as 1 GPa<sup>-1</sup>. Additionally, the initial shear modulus for the vitreous is given as  $7.6 \times 10^{-6}$  MPa in [57], which then provides  $C_{10} = 3.8 \times 10^{-6}$  MPa.

As an important note, [8] modeled the eyes as a single material quantity in their model of the human head and used different material properties. The density for the eyes in their model is listed as 1040 kg/m<sup>3</sup> with a bulk modulus of 2.19 GPa, both of which are greater than the values given in [24, 57] by around 10 percent. The much more significant difference is in the shear modulus, where [8] claims a shear modulus of 22.53 kPa for eyes, as compared to the initial shear modulus of  $7.6 \times 10^{-3}$  kPa given by [57]. These two values differ by four orders-of-magnitude, indicating that material models based on one or the other likely exhibit significantly different behavior.

## 3.2 Materials with Parameters Estimated through Optimization

### 3.2.1 Hyperelastic

In general, the hyperelastic materials were modeled with a two-term Ogden series; however, there were two notable exceptions: the walls of the bridging veins, which were treated as anisotropic hyperelastic, and the intervertebral discs, which were modeled using a Mooney-Rivlin formulation. Additionally, the assumed thickness for the various model components treated as membranes (bridging vein walls, pia mater, dura mater, and sclera) are also reported.

#### Bridging Vein Walls

The walls of the bridging veins were modeled as an anisotropic hyperelastic material. As detailed in Section 2.1.2, the Holzapfel-Gasser-Ogden model was used to characterize the walls of the bridging veins. Due to the lack of experimental data, the model parameter values were taken directly from [26]; these values are listed in Table A2. Additionally, the thickness of the bridging vein walls was specified as 120  $\mu\text{m}$  based on the work in [25].

#### Pia Mater and Dura Mater

The pia mater was modeled using experimental data from [28], which lists the density of the pia mater as 1130  $\text{kg/m}^3$ . The thickness of the pia was treated as 20  $\mu\text{m}$  based on measurements of the thickness of the pia-arachnoid complex [27]. The experimental data is shown by the solid line in Fig. 3a; however, it should be noted that this tensile stress-strain data is based on experiments originally performed by [58]. As a two-term Ogden model for hyperelasticity, a total of four unknown parameters were found using constrained nonlinear optimization, with the main constraints being the familiar stipulation for  $\mu_i$  and Drucker's first stability criterion. The final parameters for the hyperelastic model and the cost function value are given in Table A2.

The model-predicted stress is shown by the dashed lines in Fig. 3a. This figure clearly shows that the model closely matches the full range of observed experimental data. The final prediction error (cost function value) is provided in Table 3.

The dura mater was also modeled as a hyperelastic material. As with the pia mater, the density of the dura mater and its relevant mechanical properties were given in [28]. The thickness of the dura mater model was 550  $\mu\text{m}$  based on the results presented in [29]. The dura was modeled using experimental data from the same study ([28]), which is shown by the solid curve in Fig. 3b. Adopting the same approach for finding the optimal parameters as for the pia mater yielded the parameter values shown in Table A2. Additionally, the stress values generated by the models are plotted against the experimental data in Fig. 3b. This figure shows good agreement between the model and the experimental data for all strains below 18 percent, but the model begins to deviate for larger strains. This leads to a noticeable increase in the prediction error in Table 3.

#### Falx and Tentorium

The falx and the tentorium were modeled using the same material properties; the density given in Table A2 was provided by [30]. The stress-strain data used for finding the Ogden model parameters may also

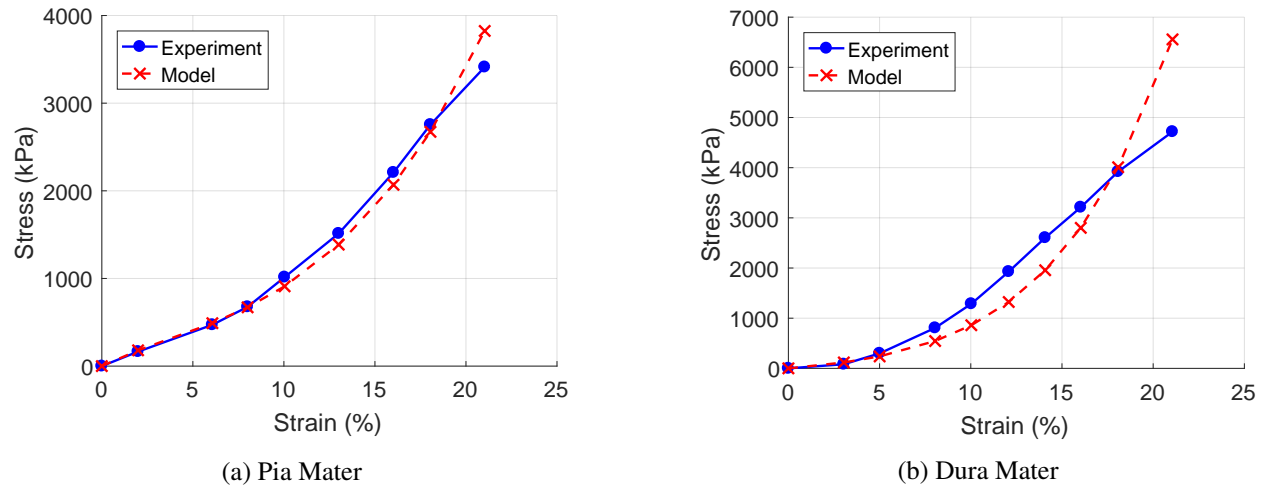


Fig. 3: Stress-strain data for the pia mater and dura mater (human subject); experimental data originally presented in [28]

be found in [30], but the data originally appeared in [59]. This experimental data is plotted in Fig. 4. Following the familiar constrained nonlinear optimization resulted in the parameter values shown in Table A2. The stress values generated by the model are plotted against the corresponding strains in Fig. 4, demonstrating reasonable agreement between the model and data. The prediction error is comparable to that for the dura mater.

### Sclera

Since little information exists about the material properties of the sclera, it was given the same density as the pia mater, which ensheathes the optic nerve; the same density for pia mater is provided in both [28] and [30]. Additionally, due to a lack of stress-strain data for the sclera, results of experimental stress-strain tests on the cornea [31] were used to calibrate the parameters of its hyperelastic model. A mean corneal thickness of  $850 \mu\text{m}$  was reported in [31], and this value was adopted for the sclera. While it is acknowledged that the cornea is separate in terms of form and function, it is continuous with the sclera and both are part of the connective tissue encompassing the globe of the eye. Thus, given their similarities and the dearth of reliable stress-strain data for the sclera, experimental data for the cornea may serve as an acceptable substitute.

The experimental data used to calibrate the sclera model, which comes from a study of the cornea, is plotted in Fig. 5. The parameters were found using the familiar optimization scheme with the same constraints, and the final parameter values are provided in Table A2. The final cost function value is shown in Table 3 to be nearly 1 percent, and the model-generated stress-strain curve in Fig. 5 is nearly indistinguishable from the original experimental data.

### Intervertebral Discs

The intervertebral discs are composed of a fluidic nucleus and fibrous annulus. For the purposes of this study, the discs were treated as a fully fibrous annulus and were modeled as a hyperelastic material using the

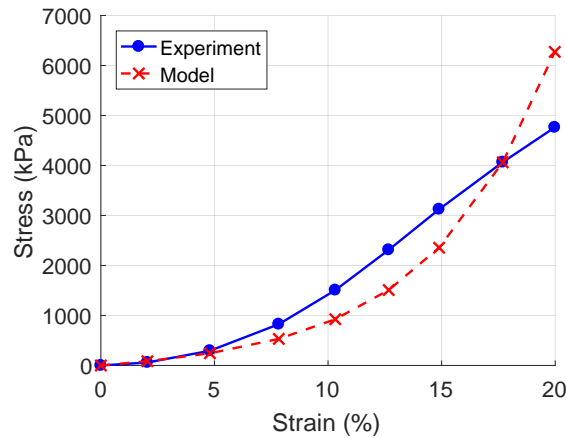


Fig. 4: Comparison of stress-strain curves for the falx and tentorium (treated as one material) based on a hyperelastic model and experimental data from [59]

Mooney-Rivlin formulation. This particular model for hyperelasticity was chosen for the discs because it has already been used to model intervertebral discs [32], and the model parameters, in addition to the mechanical and material properties for the discs, are provided in [32]. Further, no stress-strain data is available for the intervertebral discs, so a new set of parameters could not be obtained. The necessary material properties and parameters for the intervertebral discs are given in Table A2. While no bulk modulus is provided, it may be computed using Eq. (16) and the values for  $\nu$ ,  $C_{10}$ , and  $C_{01}$  reported in [32]; solving for the bulk modulus yields 4.35 MPa.

### Costal Cartilage

The costal cartilage (bars of cartilage that extend the ribs) was considered a hyperelastic material. The mechanical properties of cartilage are explored in [33], but the cartilage considered for that study is auricular cartilage (from the ear) as opposed to hyaline cartilage (from the ribs). Nonetheless, [33] provides information about the density human auricular cartilage. Based on the numerous samples collected by [33], the average wet weight for the circular punch biopsies was 35 mg, which, based on the size of the biopsies, leads to an estimated density of 1240 kg/m<sup>3</sup>. The study in [33] also assumes that the auricular cartilage is nearly incompressible; this assumption is adopted for the costal cartilage.

The experimental data used for calibrating the costal cartilage model comes the study in [33] for auricular cartilage, which serves as a useful substitute given the scarcity of biomechanical data for costal cartilage. This experimental data is shown in Fig. 6. The final parameter values were found using the familiar nonlinear optimization scheme and constraints, yielding the values shown in Table A2. When plugged back into the model, these parameters produced the “model” curve in Fig. 6 that closely follows the experimental data.

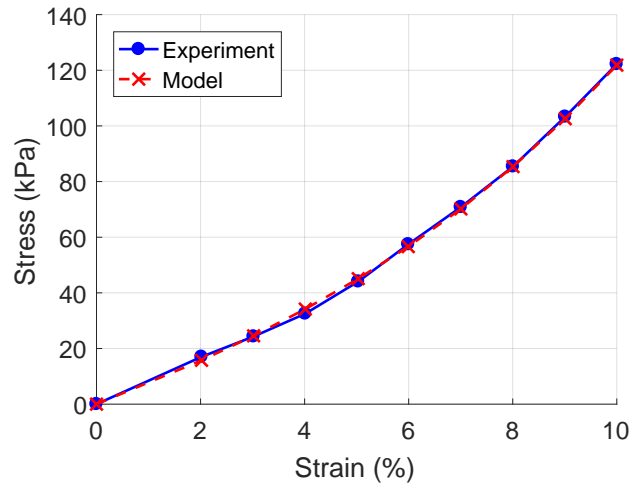


Fig. 5: Comparison of stress-strain relationship for experimental data from the cornea [31] and hyperelastic model of the sclera

Table 3: Final Cost Function Values for the Hyperelastic Materials

Component	$\bar{O}$
Pia Mater	0.0892
Dura Mater	0.2751
Falx/Tentorium	0.2622
Sclera	0.0126
Costal Cartilage	0.1107

### 3.2.2 Viscoelastic Materials

#### Bone

*Skull* — The skull is made up of two types of bone material, cortical bone and cancellous bone (also known as spongy or trabecular bone). Each of these bone materials is modeled as transversely isotropic viscoelastic, but the material properties are different (Table A3). For the cortical bone of the skull, the density and modulus information was taken from a study on the parietal bone in [34]. The density shown in Table A3 was taken as the mean of the density measurements presented in [34]; however, the modulus information required some additional manipulation of the data from [34]. When defining the transversely isotropic properties of this material, the plane of isotropy was defined along the first and second principal directions, making the third principal direction normal to the plane of isotropy. The modulus values related to the first and second principal directions, therefore, needed to be equal. This was accomplished by averaging the



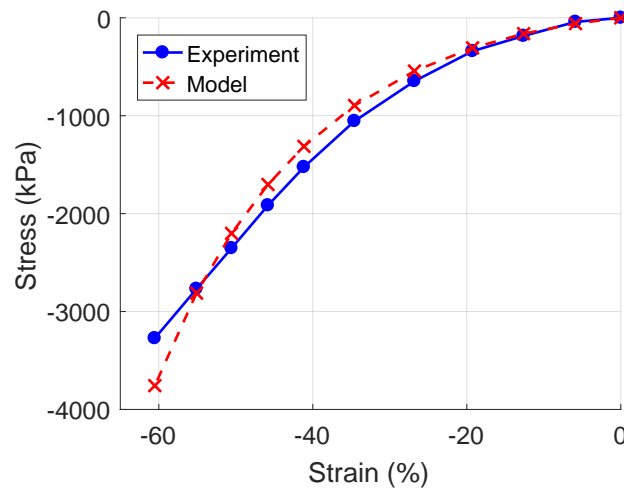


Fig. 6: Comparison of stress-strain relationship in compression for experimental data from auricular cartilage [33] and hyperelastic model of the costal cartilage

corresponding modulus values from [34]. The moduli for the third principal direction were taken directly. (As an important note, the weakest side in [34] is the first; this was changed to the third for the purposes of this study by making the appropriate changes to the modulus indices).

The Poisson's ratio values were found through a combination of analytical formulas and data from [34]. The ratio  $\nu_{12}$  was computed from the basic relation between the shear and elastic moduli shown in Eq. (57)

$$G = \frac{E}{2(1 + \nu)} \quad (57)$$

and using  $E_2$  and  $G_{12}$ ; solving for  $\nu$  yielded  $\nu_{12} = 0.30$ . The other Poisson's ratios were found by averaging  $\nu_{13}$ ,  $\nu_{23}$  and  $\nu_{31}$ ,  $\nu_{32}$ , producing 0.3975 and 0.32, respectively. According to transversely isotropic theory, the Poisson's ratios are related by  $\nu_{32}/E_3 = \nu_{23}/E_2$ ; however, given that these values come from experimental data, the ratios are only approximately the same.

The cancellous bone was more difficult to model because there is less available experimental data regarding stress and strain. However, in-depth studies on the density of human trabecular bone have been conducted in [35] and [60]. Ref. 35 performed a series of studies on the cancellous bone in lumbar vertebrae ultimately finding a bone density range of 0.057–0.142 g/cm<sup>3</sup> (57–142 kg/m<sup>3</sup>). Ref. 60 considered cancellous bone samples from the vertebrae, tibia, and femur, reporting an apparent mean density of 0.18 g/cm<sup>3</sup> (180 kg/m<sup>3</sup>) for the vertebral samples. While these values do not perfectly agree (and while it is acknowledged that the cancellous bone in the vertebrae is likely much different than that in the diploë of the skull), they offer a reasonable comparison. Ultimately a density of 100 kg/m<sup>3</sup> was chosen.

Several values for the elastic modulus of trabecular bone are presented in [60] and [61], but there is little to no agreement among the values as they span nearly a full order of magnitude. Ref. 36 offers plots

of the compressive behavior of both cortical and cancellous bone. Manual interpretation of this stress-strain data provides estimates of the elastic modulus as 16.77 GPa and 533 MPa for cortical and cancellous bone, respectively. Since this estimate of the elastic modulus of cortical bone closely resembles the values shown in Table A3, this data set was used to estimate the elastic moduli of cancellous bone. Specifically, the ratio between the two moduli  $E^{\text{cancellous}}/E^{\text{cortical}} = 0.0318$  was used to modify the elastic and shear modulus values for cortical bone listed in Table A3. The same Poisson's ratios were used because they are unaffected by a linear scaling of the modulus values. Additionally, as with the cortical bone, there was a severe lack of stress-strain data for finding the necessary viscoelastic parameters for the cancellous skull bone. Therefore, the stress-strain data from the cortical bone given in [62] was scaled by the same ratio and used for parameter estimation.

*Mandible* — The mandible bone was modeled separately from the skull using data from [34] and [37]. The mandible was modeled as a transversely isotropic viscoelastic material. The density of the mandible was taken as the approximate mean across the many samples recorded in [37]. Additionally, the elastic and shear moduli values were taken from [37]. As with the cortical bone in the skull, the plane of isotropy lies along the first and second principal directions, making the third principal direction normal to the plane of isotropy. Therefore, as before, the values related to the first and second principal directions were made equal by averaging the corresponding values from [37]. (As an important note, the weakest side in [37] is the first, but this is changed to the third for the purposes of this study).

The Poisson's ratio  $\nu_{12}$  for the mandible was, again, found by taking Eq. (57), using  $E_2$  and  $G_{12}$ , and solving for  $\nu$ , which yielded  $\nu_{12} = 0.375$ . The other Poisson's ratios were found by averaging  $\nu_{13}$ ,  $\nu_{23}$  and  $\nu_{31}$ ,  $\nu_{32}$ , producing 0.39 and 0.245, respectively. It can be shown that these Poisson's ratios generally obey the relation:  $\nu_{32}/E_3 = \nu_{23}/E_2$ .

*Vertebrae* — The vertebrae consist of cancellous bone encased in cortical bone, with cancellous accounting for 81 percent of the volume (for men) [63]. The vertebrae in the model were created using the material properties for cortical and cancellous vertebral bones in [32] and applying the rule of mixtures using the appropriate volume fractions (note that these values are slightly different than those used for the cortical and cancellous bone models). For instance, the density and elastic modulus were found through the following computations

$$\rho = 19\%(1830 \text{ kg/m}^3) + 81\%(170 \text{ kg/m}^3) = 485.4 \text{ kg/m}^3 \quad (58a)$$

$$E = 19\%(16,800 \text{ MPa}) + 81\%(100 \text{ MPa}) = 3273 \text{ MPa} \quad (58b)$$

Additionally, it was shown in [32] that the Poisson's ratio for each component of the vertebral bones was nearly  $\nu = 0.3$ ; this value was then adopted for the vertebrae in the model.

*Ribs* — The density of the ribs was taken to be the same as the density of the cortical skull bone,  $1841 \text{ kg/m}^3$ . The elastic modulus was estimated based on samples of porcine cortical bone (from the femur) in [38].

*Sternum* — The sternum is mostly cancellous bone that is encompassed by a thin layer (or shell) of cortical bone. Vertebral bones generally have the same structure, and both vertebrae and the sternum belong to the axial skeleton [64]. Considering these similarities, the sternum was modeled using the material parameters previously assigned to the vertebrae. Table A3 shows these shared properties.

*Modeling Bone* — Unlike the hyperelastic materials, only one data set was available for calibrating the viscoelastic models for all of the bone materials. The data for calibrating the models comes from [62], a study focusing on the mechanical properties, e.g., stress-strain relationship, of femoral cortical bone; there was no specific stress-strain data available for the skull, mandible, vertebrae, ribs, or sternum. The experimental data is plotted in Fig. 7 exhibiting both its linear relationship between stress and strain and the change in slope with strain rate. The experimental data covers six different strain rates spanning six decades (from  $10^{-3}$  to  $10^3$ ) but only a fairly small range of strains, as the maximum strain in the linear range was around 0.7–0.8 percent for most strain rates [62].

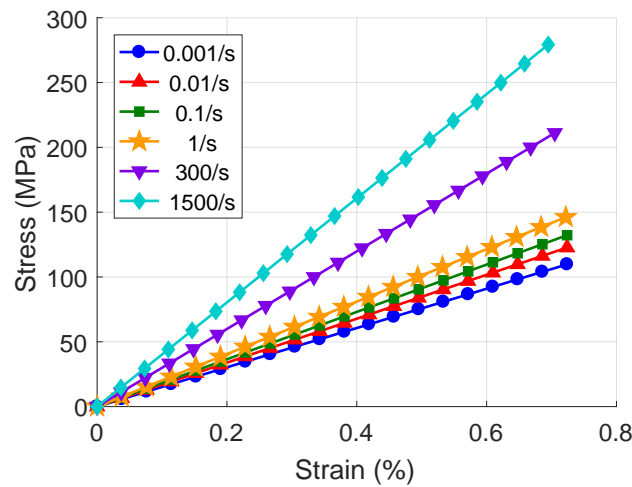


Fig. 7: Stress-strain data for femoral cortical bone at various strain rates; experimental data originally presented in [62]

The computational model has a total of six types of bone components: cortical skull bone, cancellous skull bone, the mandible, ribs, vertebrae, and sternum. For the purposes of this study, the primary differences between these bone types are their elastic and shear moduli; most of the bone materials share a Poisson's ratio of  $\nu = 0.30$ . Further Eq. (11) shows that the elastic modulus  $E$  shares a linear relationship with stress, meaning that the available experimental data set could be linearly scaled to fit each bone material. This was accomplished by normalizing the experimental data in Fig. 7 such that the slope of the curve for the highest strain rate (1500/s) was set to unity; this essentially normalized the experimental data set by the elastic modulus for the highest strain rate curve. Then, the normalized experimental data could be scaled by the elastic modulus of the material of interest, e.g., cortical skull bone or ribs, so that the 1500/s curve would have the slope (and thus elastic modulus) of the desired material. The highest strain rate curve was chosen for normalization/scaling as this was deemed the primary curve of interest. The slope (elastic modulus) of the 1500/s strain rate stress-strain curve in Fig. 7 is approximately 39.5 GPa; the various elastic moduli used for the different bone materials are listed in Table A3. It was further assumed that the available experimental data shared a Poisson's ratio of  $\nu = 0.30$ .

Given that this technique merely represents a linear scaling, it would be expected for the optimization to return essentially the same optimal parameters for the Prony series each time; any variation would likely be due to the difference in the initial parameter vector. (A small investigation revealed this assumption to be mostly true.) Therefore, it is far more efficient to fit a generic viscoelastic model to the experimental data and then perform any scaling as post-processing. Two “generic” viscoelastic models, a two-term or six-term Prony series, were fit to this data set using the nonlinear optimization scheme and constraints detailed in Section 2.3.

Given that there were data sets from six separate strain rates, a weighting vector  $\mathbf{w} = [0.5, 0.5, 0.5, 1, 2, 3]$  was used; the weights were chosen this way to emphasize the higher strain rates, as those are more commonly associated with blast effects. The final parameter values for the “generic” models are given in Table 4. It is important to note that the order of the parameters shown in Table 4 is arbitrary; each  $g_j$  and  $\tau_j$  must remain paired together, but their order may be shuffled without changing the stress computation. (Typically, the Prony series terms are presented in order of ascending  $\tau$ , but that convention does not impact the stress computation, either). The normalized total costs ( $\bar{O}$ ) are also given in Table 4, and these show that increasing the number of terms in the Prony series from two to six did not significantly reduce the error. Additionally, the parameter values for the six-term model show a great deal of redundancy in  $\tau_j$  and near-negligible values for several  $g_j$ , indicating that six terms is likely unnecessary. Therefore, the two-term model is used for the ensuing analysis as it reduced complexity did not significantly hinder its accuracy.

Table 4: Parameter Values for the Viscoelastic Model of Cortical Bone

Prony Series Model		$g_j$	$\tau_j$	$\bar{O}$
2-term model	$j = 1$	0.4838	$1.32 \times 10^{-5}$	0.4124
	$j = 2$	0.1336	$6.00 \times 10^{-2}$	
6-term model	$j = 1$	0.0186	$8.73 \times 10^{-1}$	0.3858
	$j = 2$	0.0175	$8.73 \times 10^{-1}$	
	$j = 3$	0.0180	$8.78 \times 10^{-1}$	
	$j = 4$	0.0176	$8.75 \times 10^{-1}$	
	$j = 5$	0.0792	$1.56 \times 10^{-2}$	
	$j = 6$	0.4772	$1.29 \times 10^{-5}$	

The modeling of the skull was divided into two parts, cortical bone and cancellous bone. The stress-strain curves the cortical skull bone were generated using the two-term model and plotted against the appropriately scaled experimental data in Fig. 8; for scaling, the cortical skull bone was given an elastic modulus of 16.65 GPa, which is also the slope of the 1500/s stress-strain curve. For the lower strain rates, shown in Fig. 8a, the model-predicted curve had a fairly small but consistent deviation from the experimental data. The model essentially matches the experimental curve for  $0.001 \text{ s}^{-1}$  strain rate but is less exact for the other low strain rates. Figure 8b demonstrated that the model-predicted curves generally followed the experimental results, especially for the strain rate of  $1 \text{ s}^{-1}$ .

Modeling of the cancellous skull bone required a more drastic scaling of the data, as the elastic modulus for the cancellous skull bone was roughly 3.18 percent of that for the cortical skull bone (530 MPa/16.65 GPa). The model-predicted stress values are plotted against the ratio-adjusted experimental results in Fig. 9. As with the cortical bone plots, the slope of the 1500/s stress-strain curve is set to 530 MPa.

Figures 8 and 9 demonstrate that each stress-strain plot for a bone material is essentially the same save the scaling of the stress. Thus, there is little need to plot the model comparisons for the bone materials as the plots are the same each time, only scaled. For this reason, the comparison plots for the ribs, sternum, and vertebrae are not included; the relevant material properties for these materials are given in Table A3 and the viscoelastic parameters, i.e., the Prony series terms, remain the same as for cortical and cancellous skull bone. The one material exception is the mandible, which has a Poisson's ratio of  $\nu = 0.375$ , which is significantly different enough to require a slightly modified model.

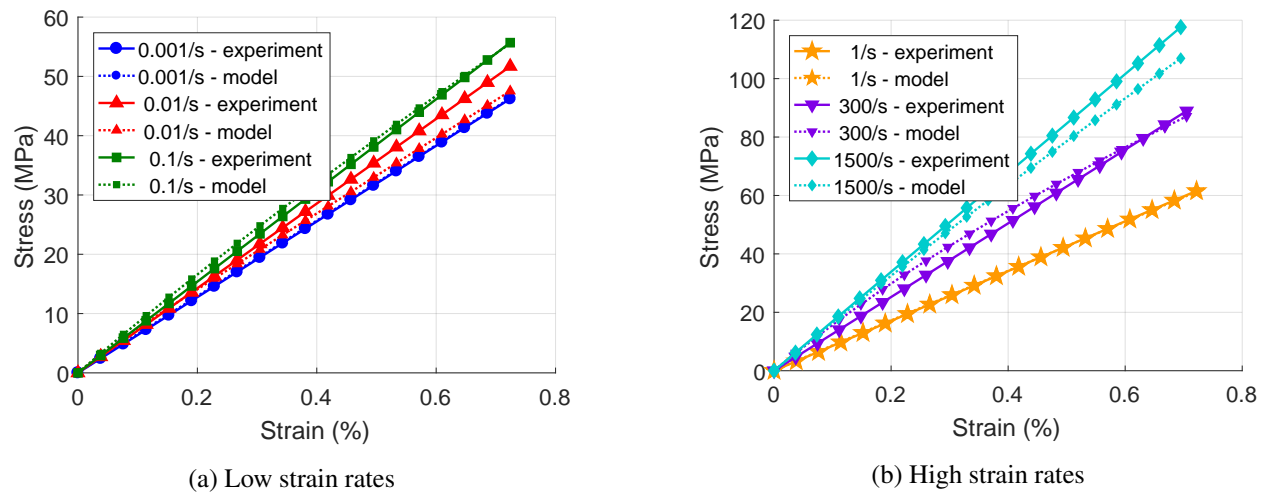
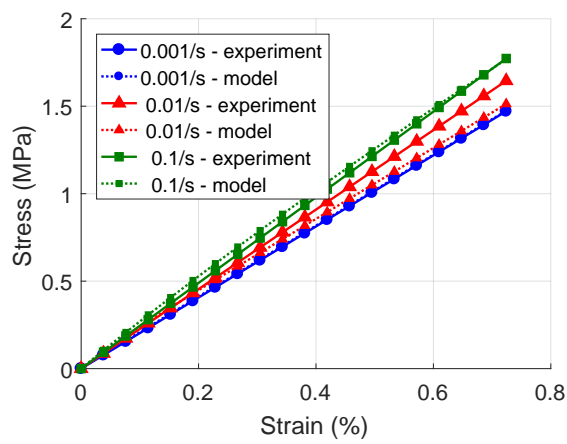
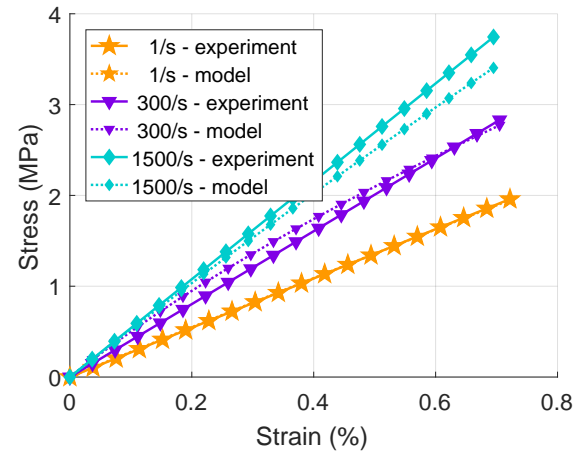


Fig. 8: Comparison of stress-strain curves produced from scaled experimental data of cortical bone [62] (solid lines) and viscoelastic model of cortical skull bone (dashed lines)



(a) Low strain rates



(b) High strain rates

Fig. 9: Comparison of stress-strain curves produced by scaled experimental data of cortical bone [62] (solid lines) and viscoelastic model of cancellous skull bone (dashed lines)

The model parameters for the mandible are given in Table A3, but it may be easily seen that they are identical to those for the generic model (albeit in a different order); similarly, the final normalized total cost was the same. This can be easily understood by the fact that Eq. (11) demonstrates that the Poisson's ratio  $\nu$  does not factor into the uniaxial stress calculation for a linear viscoelastic model. Figure 10a shows that the model-predictated stresses for the lower strain rates evince the same degree of accuracy as in the cortical and cancellous skull bone plots; the same is also true for the plots of the higher strain rates. While the optimization of parameter values for the mandible model may seem like a redundant and unnecessary task, the optimization was nonetheless performed because the difference with respect to  $\nu$  would be cause for determining different parameter values if a model that incorporated Poisson's ratio were to be used. Additionally, the results of an optimization trial over a scaled model revealed the relative insensitivity of the parameter values, suggesting that a unique parameter value set exists for the two-term Prony model for bone materials.

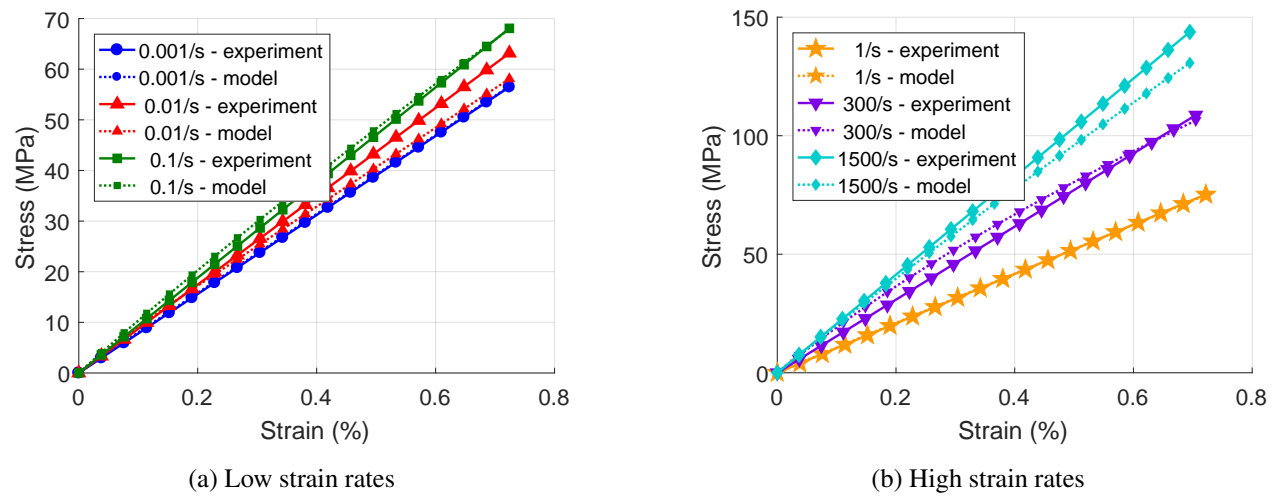


Fig. 10: Comparison of stress-strain curves produced by scaled experimental data of cortical bone [62] (solid lines) and viscoelastic model of mandible bone (dashed lines)

### 3.2.3 Hyper-viscoelastic

#### Cerebrum, Cerebellum, Brain Stem, Spinal Cord, and Optic Nerves

The cerebrum and cerebellum are both composed of grey matter and white matter, each of which must be treated as a separate material. Both grey matter and white matter were considered to be hyper-viscoelastic materials. The densities of grey and white matter, as reported in [8], are given in Table A4. In addition to the cerebrum and cerebellum, the various parts of the brain stem, the spinal cord and the optic nerves were all modeled as hyper-viscoelastic materials. Since the brain stem and spinal cord are primarily composed of white matter, those model components adopted the parameters estimated for the white matter of the

cerebrum and cerebellum. Based on the work by [65], the optic nerve may be assumed to behave similarly to central nervous system tissue, e.g., white matter. Therefore, the optic nerve was also modeled using the same constitutive equations and materials properties as for white matter.

The parameters for the hyper-viscoelastic models of the grey and white matter were found through calibration using data from [66]. The experimental stress-strain data for porcine grey matter is shown in Fig. 11, demonstrating how strain rate impacts the stress. (Note that the data in Fig. 11 is for compressive stress-strain testing.) The strain rates vary by at least five orders of magnitude between Figs. 11a and 11b. In turn, the observed stresses vary by two or three orders of magnitude; however, Fig. 11b shows that for very high strain rates, the stress can increase by nearly an order of magnitude when tripling the strain rate. For the slower strain rates in Fig. 11a, a ten-fold increase in strain rate only results in the three- or four-fold increase in stress. Clearly, though, the effect of strain rate has an important influence on the model parameters.

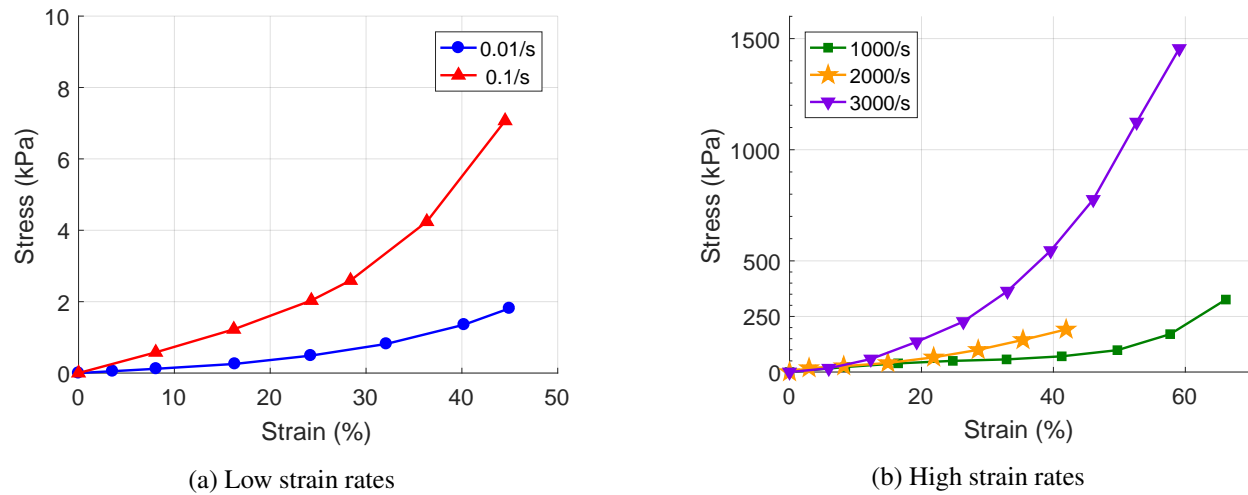


Fig. 11: Grey matter stress-strain data for various strain rates (porcine subject); experimental data originally presented in [66]

Since curves for multiple strain rates are included in the calibration data, there was an additional consideration of weighting the five data sets. Ultimately a weight vector  $\mathbf{w} = [0.5, 1, 2, 1, 0]$  was chosen. Thus, the data from the test with a strain rate of 1000/s was deemed most important, and the data from the test with a strain of 3000/s was ignored during parameter estimation. The final parameters returned by the optimization scheme for the hyper-viscoelastic model of grey matter are listed in Table A4. The optimal parameter reveal that the Prony terms were rather insensitive to the data, as one term clearly became dominant. For the Ogden terms, the hyperelastic behavior is dominated by a near-cubic term ( $\alpha_2 = 2.74 \approx 3$ ).

Figure 12 shows the stress-strain curves generated by the hyper-viscoelastic model of grey matter for the various strain rates. For the lower strain rates in Fig. 12a the model-predicted stress generally followed the experimental data up to the maximum strain around 45 percent for both sets of curves. The same observation



could be made for some of the higher strain rates; however, the model-predicted stress for the 3000/s strain rate appears to deviate from the experimental data quite rapidly for strains in excess of 15–20 percent. Across all strain rates, Fig. 12 demonstrates that the model provides sound estimates for strain rates up to 2000/s for strains up to 45–50 percent. While the model does not perform as well for the strain rate of 3000/s, it is important to recall that this data set was given zero weight during optimization.

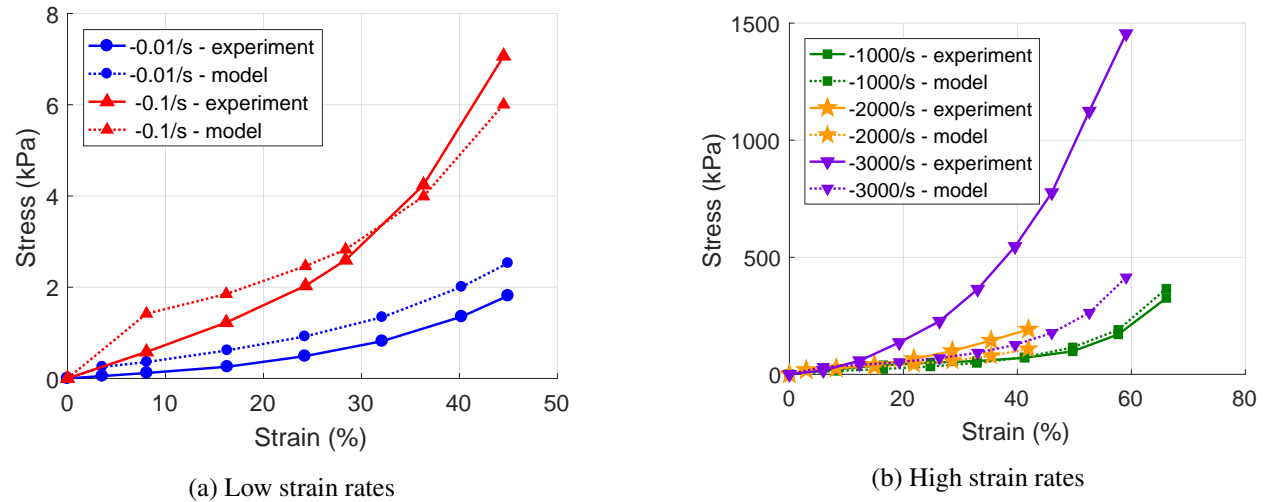


Fig. 12: Comparison of experimental stress-strain data and hyper-viscoelastic model for grey matter for various strain rates (procine subject); experimental data originally presented in [66]

The plots in Fig. 12 only show the model-predicted compressive stresses (which are treated as positive), but Fig. 13 exhibits the model-predicted stresses from  $-30$  percent to  $30$  percent strain to include both compression and tension. (Please note that compressive stress and strain are treated as negative in Fig. 13.) A variety of strain rates spanning three orders of magnitude are included in Fig. 13 to capture the full range of stress-strain behaviors exhibited by the model. This figure demonstrates that the model produces a rather severe increase in stress for very small strains for larger strain rates — evidence of this sharp rise may also be observed in the 0.1/s curve in Fig. 12a. This sharp rise in stress may be due in part to the modeling assumption of a constant strain rate when, in fact, critical studies of Hopkinson Bar tests have revealed that this experimental technique, which was used to produce the results in [66], does not actually result in a constant strain rate, especially for the lower strains at the initiation of the experiment [67].

White matter was modeled in the same manner as grey matter, using data sets from the same source [66]. Figure 14 presents the experimental stress-strain data for porcine white matter. The data in these figures was used to determine the optimal parameters for the hyper-viscoelastic model for the white matter. The same optimization scheme was used with the same weighting vector applied to the experimental data. Additionally, the same constraints were applied to the model parameters.

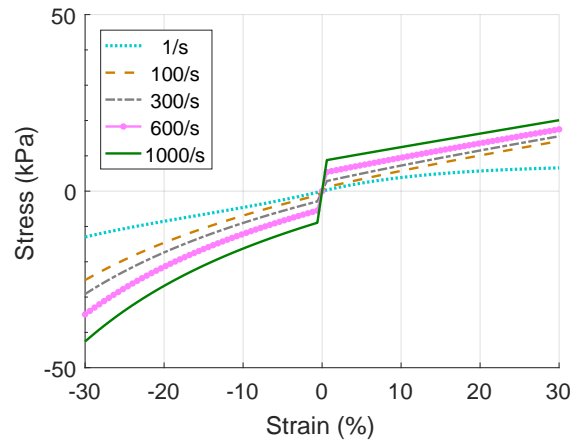


Fig. 13: Model-predicted stress for grey matter over a strain range of  $[-30\%, 30\%]$  for a variety of strain rates

The resulting model parameters produced by the optimization algorithm are given in Table A4. Both the parameters for the Ogden and Prony terms are noticeably different from those for the model for grey matter. Most notably, the shear modulus parameters differ by an order of magnitude and the Prony series is not completely dominated by a single term for white matter. The values for the normalized cost function are also shown in Table 5, and they present a stark contrast between the grey matter and white matter; namely, the normalized prediction error, i.e., the final cost function evaluation, is much larger for grey matter. However, this difference is most likely the result of the randomness associated with solving a high-dimensional optimization problem.

While the global search algorithm seeks to find the global minimum among a large population of local minima, there is no guarantee that the global minimum will be found (as was shown with the sample material). Further, this method, despite its use of multiple trial points, retains at least some sensitivity to initial conditions. Additionally, given that the optimization is based on minimization with respect to experimental data, it is highly possible (if not likely) that a unique solution does not exist because the data does not strictly conform to the model; also, different data sets were used for grey and white matter, and it is possible that the data set for white matter better fits the assumed model. Therefore it is possible that additional attempts with the global search could produce an optimal parameter set with a lower prediction error, but it is also possible that another global search would find an optimal parameter set with higher prediction error.

The model predictions for the white matter are plotted against the experimental data in Fig. 15. The improvement in normalized prediction error is reflected in Fig. 15a where both of the model predictions for the low strain rates nearly match the experimental data. The curve for 0.01/s strain rate begins to show some deviation around 50–60 percent strain, but this is still rather small. The model predictions for the 1000/s strain rate nearly perfectly follow the experimental data in Fig. 15b, whereas the predictions for the higher strain rates of 2000/s and 3000/s are not quite as close but still comparable for 2000/s. In comparison to the grey matter model predictions, those for the white matter are slightly better for the low strain rates but noticeably better for the higher strain rates around 2000/s and 3000/s.

The model-predicted stress-strain curves for white matter over the  $[-30\%, 30\%]$  strain range are provided in Fig. 16. The most obvious observation is that the stress in white matter is much larger than it is in

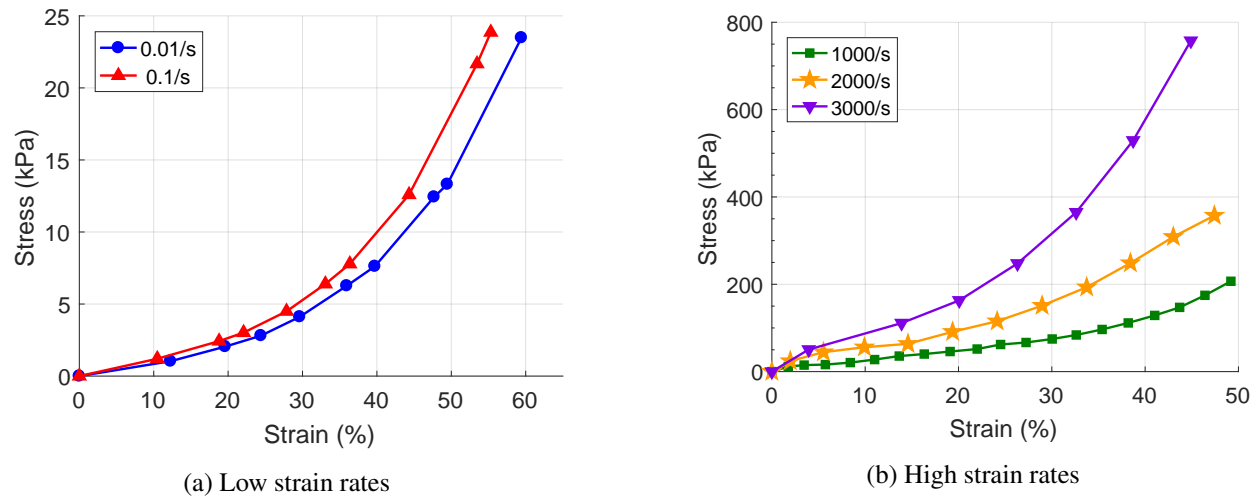


Fig. 14: White matter stress-strain data for various strain rates (procine subject); experimental data originally presented in [66]

grey matter for similar strains, but this could also be observed by comparing Figs. 11 and 14. As with the grey matter, there is a drastic increase in stress for the small strains. However, unlike the curves for grey matter, the transition to small increases in stress is not nearly as sharp. Additionally, for positive strain rates, i.e., those in tension, the curves for white matter evince a more asymptotic behavior with increasing strain.

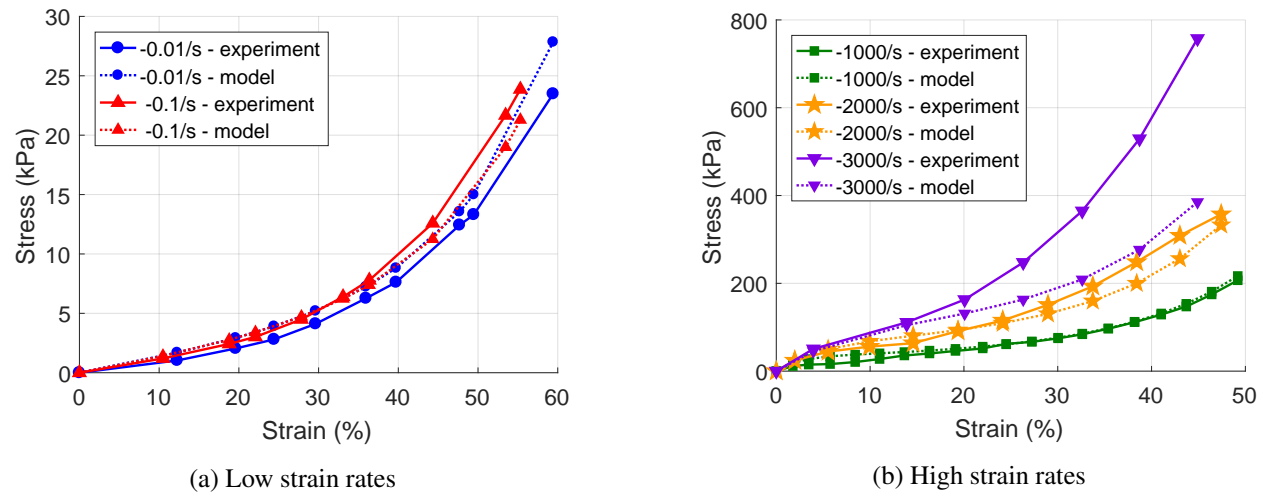


Fig. 15: Comparison of experimental stress-strain data and hyper-viscoelastic model for white matter for various strain rates (procine subject); experimental data originally presented in [66]

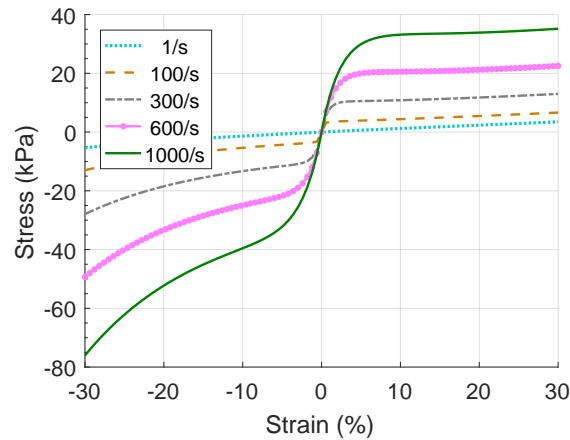


Fig. 16: Model-predicted stress for white matter over a strain range of  $[-30\%, 30\%]$  for a variety of strain rates

## Skin

The skin for the model was treated as a hyper-viscoelastic material. The density of a human scalp is given in [39] (see Table A4), and a bulk modulus for a combined material of skin and fat is provided by [8]. Since no other bulk modulus for skin was available, the combined bulk modulus is used. The other material properties necessary for calibrating the hyper-viscoelastic skin model, namely the stress-strain relationships, come from tests on porcine samples.

The parameters for the skin model were found using test data from two studies, [68] and [69]. However, one study focused on testing the skin in compression [68] while the other presents results for tensile tests [69]. The experimental test data from these papers was extracted and aggregated into one larger set, as shown in Fig. 17, where the negative strain rates denote compressive tests; in order to ensure continuity around 0 percent strain, a smoothing filter was applied to the extracted data. Figure 17 exhibits the vast difference in stress between the compressive and tensile tests, as the compressive stresses are significantly larger than the tensile stresses; this is true across all strain rates.

The data set used for calibrating the material model was a subset of that shown in Fig. 17 as only the following strain rates were included:  $-0.40/s$ ,  $0.50/s$ ,  $-40/s$ ,  $1700/s$ ,  $2500/s$ ,  $-4000/s$ . This subset of six strain rates was considered representative of the total data set while also providing a necessary focus on higher strain rates, which are often associated with TBI and blast load modeling. The weight vector for the selected strain rates was chosen as  $\mathbf{w} = [0.5, 1, 2, 3, 1, 0.5]$ , placing the greatest weight on the  $1700/s$  data set and the least weight on the extremes from the compressive testing. The skin was modeled as a hyper-viscoelastic material with a two-term Ogden series and two-term Prony series. The final parameters produced by the global search are given in Table A4.

There is not much information to be gleaned from the parameter values themselves, other than the fact that the skin model does not appear to have any single dominant term. The normalized prediction error is larger than that for both grey and white matter, but Fig. 18 demonstrates that the overall fit for the

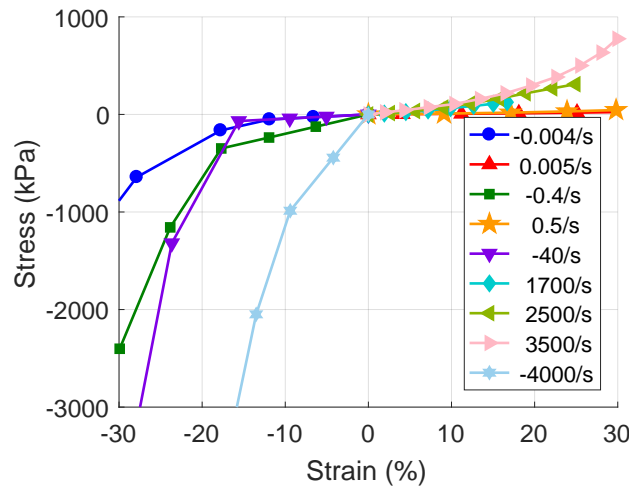


Fig. 17: Compressive and tensile stress-strain data for porcine skin at various strain rates; experimental data originally presented in [68] (compression) and [69] (tension)

experimental data is rather strong. For both the compressive and tensile strain rates, the model captures the general stress behavior. Comparing Figs. 18a and 18b shows that the model more closely follows the trajectories for the tensile experimental data, but the model still approximates the global behavior of the compressive experimental data quite well.

Stress-strain curves for various strain rates are plotted in Fig. 19 over a range from  $-30$  percent to  $30$  percent strain. The main observation from this figure is that a given level of strain produces a much larger stress for strain rates at or above  $100/s$ ; however, the stress-strain curves quickly converge for the higher strain rates. Also, the stress-strain behavior greatly differs in tension and compression with the compressive strains resulting in much large stresses. Note that it is highly likely that this is not the true expected behavior; however, these plots represent the best estimate considering the currently available data.

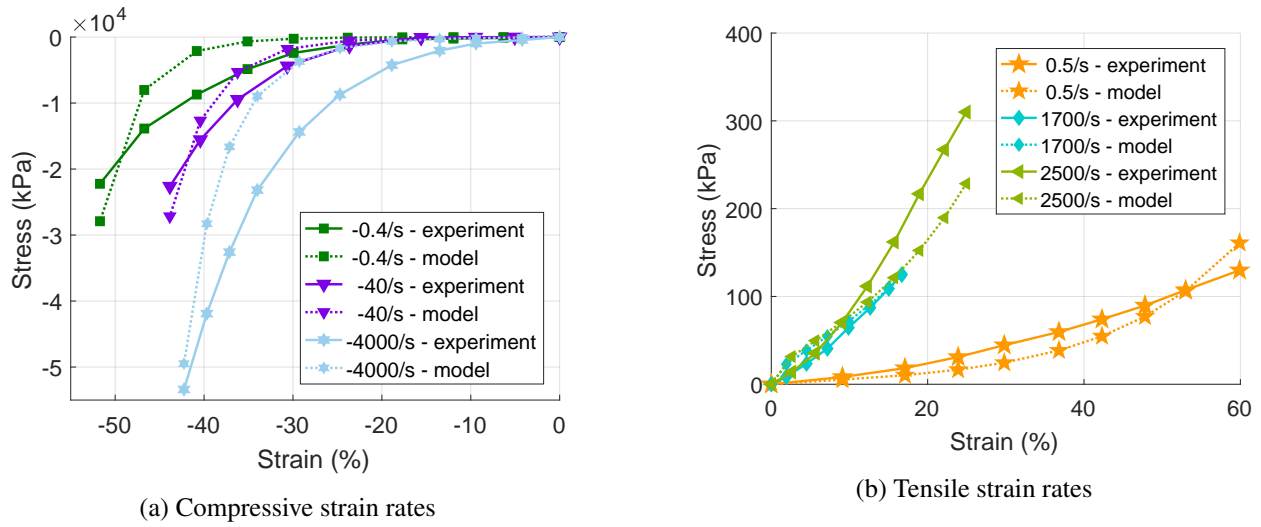


Fig. 18: Comparison of experimental stress-strain data and hyper-viscoelastic model for skin for various strain rates (procine subject); experimental data originally presented in [68] (compression) and [69] (tension)

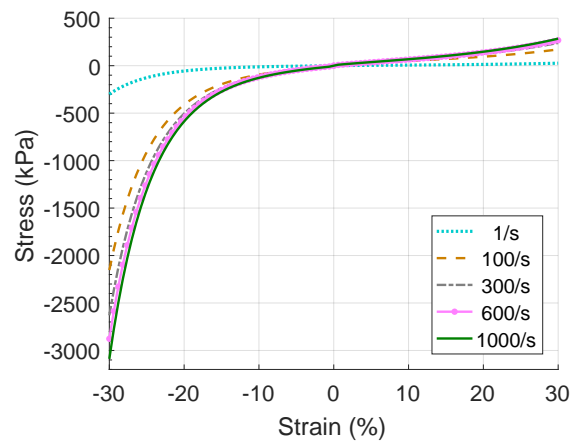


Fig. 19: Model-predicted stress for skin over a strain range of [-30%,30%] for a variety of strain rates

## Heart

The density for the heart model was based on densities reported for skeletal muscle as no data was available specifically for heart density. The average density of muscle in 4 percent and 37 percent formaldehyde solutions were reported as  $1112 \text{ kg/m}^3$  and  $1055 \text{ kg/m}^3$ , respectively, [40]; whereas muscle was given a general density of  $1100 \text{ kg/m}^3$  in [8]. The muscle density chosen for this study was  $1060 \text{ kg/m}^3$ , as shown in Table A4. Ref. 8 also provides a bulk modulus for muscle of  $3.33 \text{ MPa}$ .

The experimental data used for the model parameters for the heart comes from a study of the porcine aortic heart valve [70]. The stress-strain data from those tensile tests is plotted in Fig. 20. As Fig. 20 shows, the stress-strain data only covers low strain rates. Further, the stress-strain curves display a sudden, albeit brief, decrease in stress, giving the curves a rather jagged appearance. This sudden decrease was noted by [70] but not attributed to any specific factor. Prior to optimization it was unknown what effect, if any, these sudden decreases would have on parameter estimation.

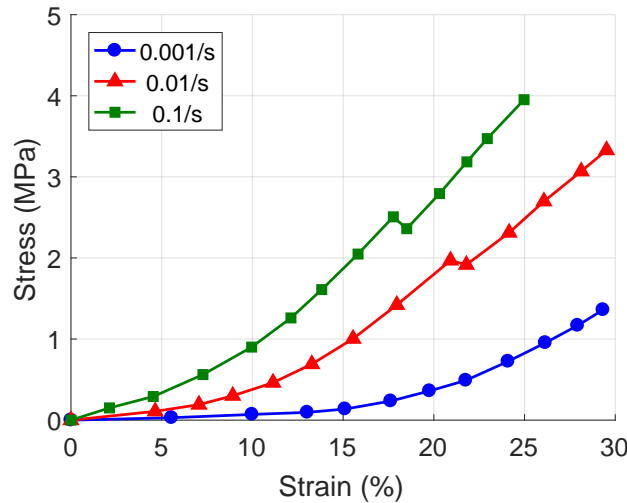


Fig. 20: Tensile stress-strain data for a porcine aortic valve at various strain rates; experimental data originally presented in [70]

Since only three data sets were available, all were used when calibrating the model parameters and each was given equal weight, i.e.,  $w_i = 1$ . The hyper-viscoelastic model for the heart had two terms for both its Ogden series and Prony series. The parameter values returned by the optimization are given in Table A4. Interestingly, the values for both  $\alpha$  terms are quite large and time constants represent two relative extremes: a constant greater than unity and the other approaching an infinitesimally small quantity. The normalized prediction error shown in Table 5 implies relatively accurate predictions, and these are illustrated in Fig. 21.

From Fig. 21 it may be seen that the model predictions closely follow the original experimental stress-strain curves. Notably, the model could not account for the sudden decrease in stress; the model appears to offer a more averaged prediction instead. Despite the lack of this particular feature, the model provides



relatively accurate (and stable) predictions of the stress all the way to 30 percent, the maximum strain considered.

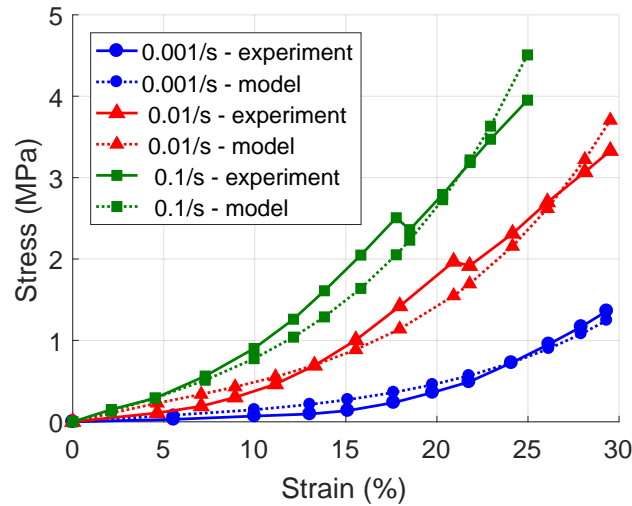


Fig. 21: Comparison of experimental stress-strain data and hyper-viscoelastic model for the heart for various strain rates (procine subject); experimental data originally presented in [70]

Plotting stress-strain curves for various strain rates, as in Fig. 22, reveals that they essentially trace over one another. The curves in Fig. 21 evinced necessary separation, but those plots were for strain rates below 1/s; once the strain rates reach or surpass 1/s, they have converged to the same trajectory. The reasons for this are most likely associated with the lack of strain data for higher strain rates, but these higher strain rates are of interest due to their association with blast loading.

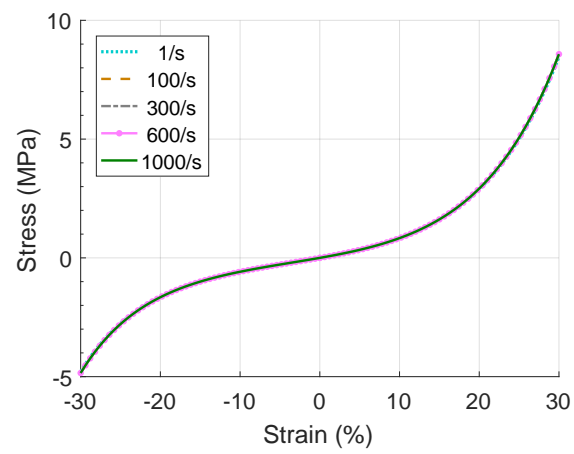


Fig. 22: Model-predicted stress for the heart over a strain range of  $[-30\%, 30\%]$  for a variety of strain rates

## Lungs

The lungs were also modeled as a hyper-viscoelastic material. While [42] offer information about the Poisson's ratio of the lungs,  $\nu = 0.43$ , their work contains a limited amount of stress-strain data, data that originated from the work of [71]. Additional stress-strain data from higher strain rates is available for porcine lungs in [72].

Specific information about the density was reported in [41]. While [41] provides an exhaustive investigation of lung density before and during general anesthesia with numerous samples collected at several locations within the lungs, this current study only needs a single value. Therefore a lung density of  $0.235 \text{ g/cm}^3$  ( $235 \text{ kg/m}^3$ ) was chosen based on a simple average of the horizontal density profiles for the right and left lungs. A bulk modulus for the lungs could not be found in the literature.

The model parameters for the lungs were found using experimental data from [42] and [72]. The experimental data included both tensile [42] and compressive [72] strain rate data sets, as shown in Fig. 23. Note that the tensile data set was taken from human tissue whereas the compressive experimental data was from porcine lung tissue. Data coming from disparate sources is an obvious source of potential error, but for the purposes of this study, these data sets may be considered together.

In terms of the stress-strain curves, one important observation is that the stress magnitudes between the tensile and compressive data sets differ by one or two orders of magnitude. This problem was similarly encountered for the skin tissue but did not ultimately lead to any problems with the optimization. Additionally, the behavior of the lung tissue differs between being in tension or compression, as the tensile data show a near linear relationship between stress and strain, but the compressive data is significantly more nonlinear.

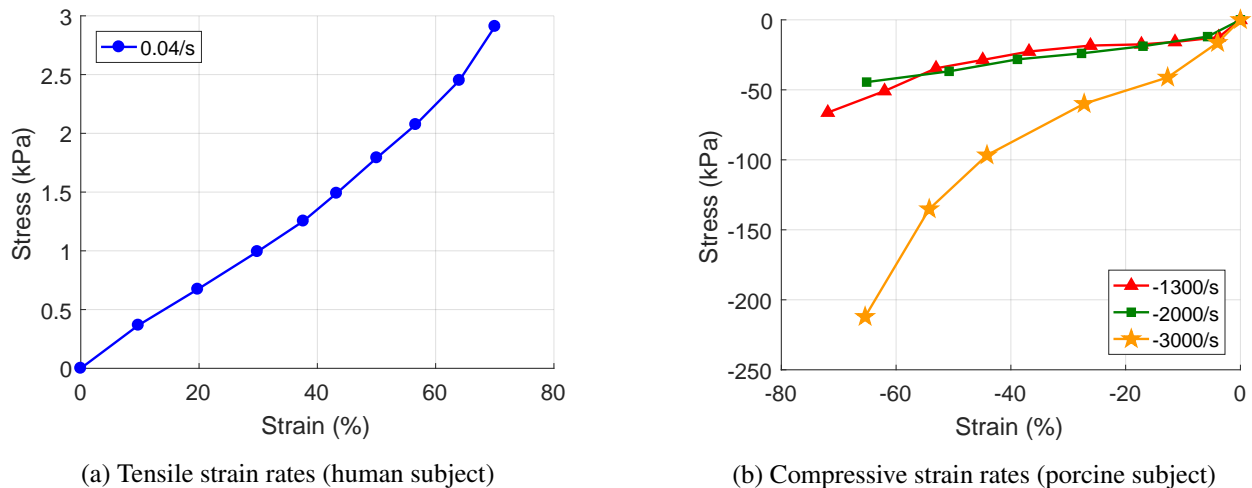


Fig. 23: Compressive and tensile stress-strain data for lung tissue (human and porcine) at various strain rates; experimental data originally presented in [42] (tension) and [72] (compression)

The material model for the lungs included a two-term Ogden model and a two-term Prony series. Prior to optimization, the four data sets shown in Fig. 23 were given the following weighting vector  $\mathbf{w} = [1, 3, 2, 1]$  corresponding to the strain rates of  $[0.04/\text{s}, -1300/\text{s}, -2000/\text{s}, -3000/\text{s}]$ ; as with other materials, the data for the strain rate closest to  $1000/\text{s}$  was given the greatest weight and, thus, largest influence on the optimization. The optimal parameter values are shown in Table A4. It should be noted that the lungs proved especially difficult to model as two optimization trials could result in predictions errors close to 1, i.e.,  $\approx 100\%$  error, and 1500, i.e.,  $\approx 150,000\%$  error; the results shown in Table A4 (with the associated prediction error in Table 5) came after only a few trials. The difficulties associated with the optimization of these biomaterials was previously discussed at length; however, the uniquely challenging case for the lung tissue merits special mention.

The individual parameters for the lung model are not particularly noteworthy with the exception of the more equal “weight” of the Prony terms with  $g_1 = 0.5802$  and  $g_2 = 0.4187$ . Most of the materials discussed previously showed a much greater imbalance in their modulus ratios. However, the relative balance for this case did not contribute to a particularly accurate result as the normalized prediction error was 47.53 percent. Figure 24 illustrates this larger error as the model-predicted stress-strain curve for the tensile strain rate is too linear and the model predictions for the compressive strain rates begin to diverge from their experimental curves for large strains. The stress-strain curve for the  $-1300/\text{s}$  strain rate is closely followed along its trajectory, but it was given the greatest weight during optimization. Overall, the model parameters for the lung tissue provide an effective and reasonably accurate prediction of the experimental data.

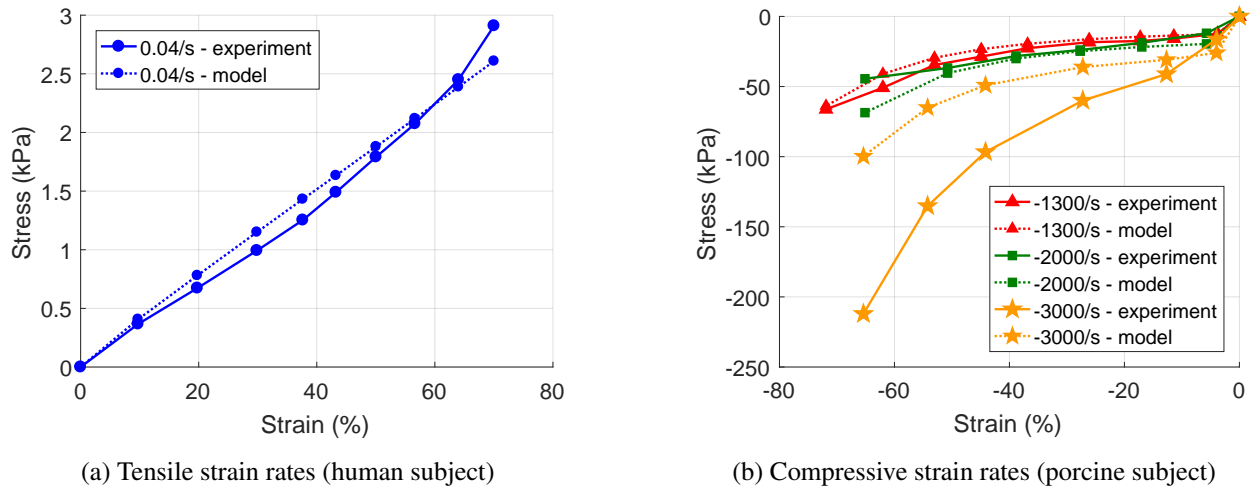


Fig. 24: Comparison of experimental stress-strain data and hyper-viscoelastic model for lung tissue for various strain rates (both human and porcine subjects); experimental data originally presented [42] (tension) and [72] (compression)

The stress-strain behavior for several strain rates is plotted in Fig. 25 over a range spanning  $-30$  percent to  $30$  percent strain. These plots demonstrate the rather consistent behavior of the lung model for increasing

strains and strain rates. As the strain rates increase, the curves in Fig. 25 exhibit a steady progression; the curve for 1000/s produces the largest stresses for a given strain, without displaying any obvious signs of convergence. Also, Fig. 25 provides more evidence for a trend previously observed for the white matter model, and to a lesser extent for the skin model, that tensile strains lead to an asymptotic increase in stress but compressive strains lead to a continual increase in stress.

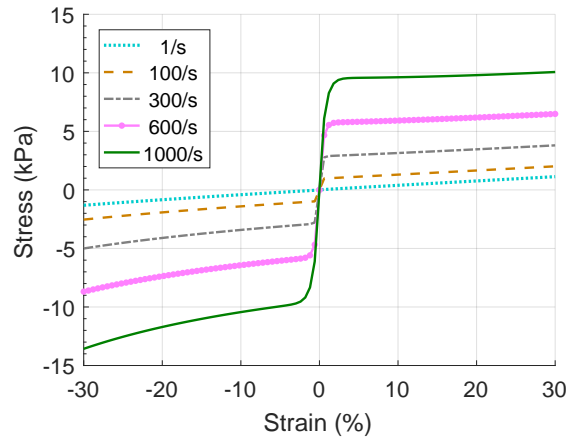


Fig. 25: Model-predicted stress for the lungs over a strain range of  $[-30\%, 30\%]$  for a variety of strain rates

## Muscles

As was detailed for the modeling of the heart, muscle density was given in [40] as ranging between  $1055 \text{ kg/m}^3$  and  $1112 \text{ kg/m}^3$  depending on formaldehyde concentration and was given in [8] as  $1100 \text{ kg/m}^3$ . As with the heart material model, a density of  $1060 \text{ kg/m}^3$  was chosen for muscle. Ref. 8 also provided a bulk modulus for muscle of  $3.33 \text{ MPa}$ , which is the same as was used for the heart.

Data for modeling the muscles came from both [73] and [74]; as with previous model components, two data sources were consulted because one provided strain data in compression [73] and the other in tension [74]. Across the two data sources, ten distinct strain rates were tested, spanning the very slow rates ( $-0.007/\text{s}$ ) to the very fast ( $-3700/\text{s}$ ), and the stress-strain curves for all of these strain rates are plotted in Fig. 26. As has been observed previously, the compressive stresses are larger in magnitude their tensile counterparts for similar strains. In addition, the tensile stresses evince some asymptotic behavior with increasing strains beyond 20–30 percent, whereas the compressive strains exhibit no such behavior. The two data sets also appear to have a relatively smooth transition through 0 percent strain for low strain rates; the transition is much more abrupt for higher strain rates.

Given that there was such a large collection of data, not all were included in the calibration of the model parameters. The chosen weighting vector was  $\mathbf{w} = [0.5, 0, 1, 0, 3, 2, 1, 1.5, 0, 0]$ , which included six data sets:  $-0.007/\text{s}$ ,  $-0.07/\text{s}$ ,  $-540/\text{s}$ ,  $700/\text{s}$ ,  $1400/\text{s}$ , and  $-1900/\text{s}$ . Using the selected data sets, the global search algorithm was used to find the optimal parameters. The final parameters are given in Table A4 and

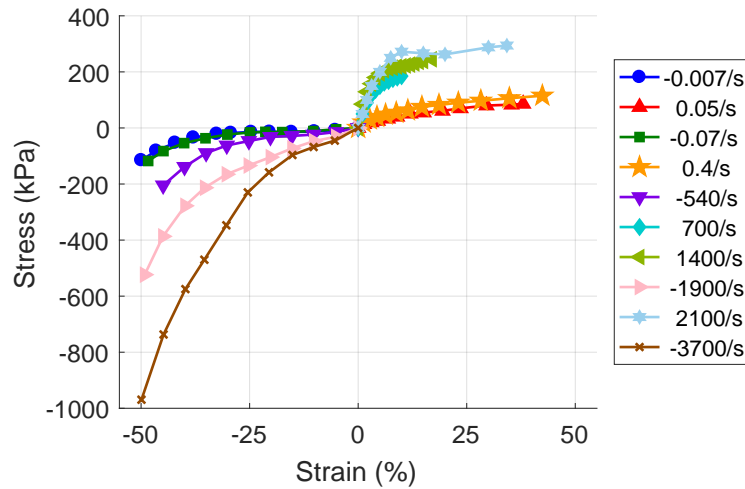


Fig. 26: Compressive and Tensile stress-strain data for porcine muscle at various strain rates; experimental data originally presented in [73] (compression) and [74] (tension)

the normalized prediction error is listed in Table 5. The error is rather large, but this is likely due to the somewhat incongruous tensile and compressive data sets.

Figures 27 and 28 elucidate some differences between the two data sets that cannot be as readily observed in Fig. 26. For instance, the behavior of the tensile data changes more significantly with increasing strain rate; the compressive data seems to exhibit a steady progression with increasing strain rate, but the tensile data set is not nearly as consistent. A brief investigation was conducted in order to better quantify this inconsistency; another trial for global search was run without including any tensile data, i.e.,  $w_i = 0$  for all tensile data sets including 700/s and 1400/s. This resulted in a normalized prediction error of less than 5 percent ( $\bar{O} = 0.0450$ ) and produced model predictions there were incredibly close to the experimental compressive data. However, if those model parameters were used in conjunction with the original weighting vector that included two tensile data sets, the prediction error ballooned to 2.1876.

This shows that omitting the tensile data could lower the error during optimization but would ultimately lead to a worse fit for the *overall* data set. Figures 27 and 28 demonstrate the model predictions produced with parameters in Table A4 produced reasonable estimates for the tensile data and relatively accurate estimates for the compressive data; this was especially true for the lower strain rates. Even though the result shown in Table 5 boasts an error in excess of 100 percent, the plots comparing the model predictions to the experimental data reveal that the estimates are of much higher quality that the bulk error measure would imply.

Plotting stress-strain curves across compressive and tensile strains, as in Fig. 29, demonstrates that the model for the muscle tissue responds similarly in tension and compression. Unlike some of the other materials, the muscle model does not exhibit any asymptotic behavior, in either tension or compression. The curves in Fig. 29 also do not show any signs of convergence, and the separation in curves over strain rate decades appears to grow as the curves for 1/s and 100/s are much closer than those for 100/s and 1000/s.

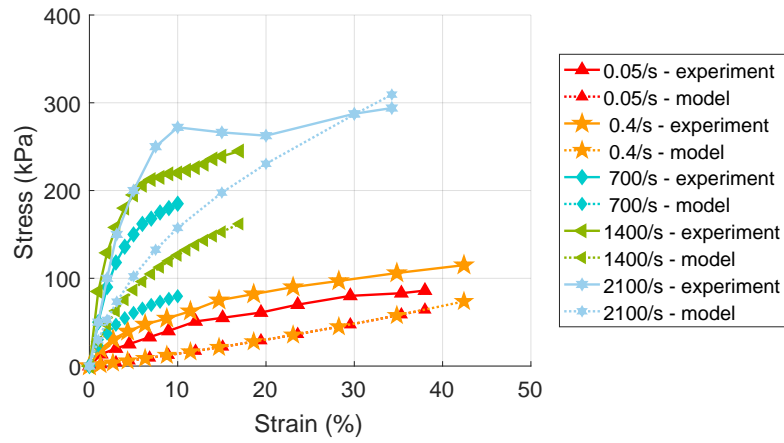


Fig. 27: Comparison of experimental stress-strain data and hyper-viscoelastic model for porcine muscle in tension at various strain rates; experimental data originally presented in [74]

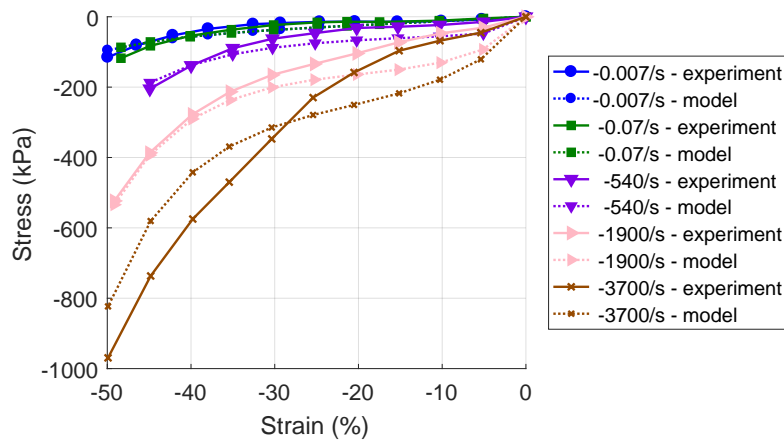


Fig. 28: Comparison of experimental stress-strain data and hyper-viscoelastic model for porcine muscle in compressive at various strain rates; experimental data originally presented in [74]

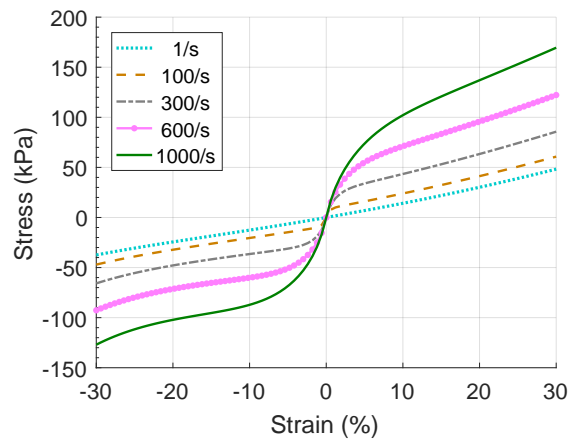


Fig. 29: Model-predicted stress for muscle tissue over a strain range of  $[-30\%, 30\%]$  for a variety of strain rates



## Adipose

No bulk properties for adipose tissue were found in the literature; however, [8] presents a bulk modulus for the skin and fat of a human, and that bulk modulus is adapted for modeling the adipose tissue in this study. The density of skin and fat is also presented in [8] as  $1040 \text{ kg/m}^3$ , but [39] asserts the density of skin as  $1200 \text{ kg/m}^3$ ; this study adopts the more dense estimate.

The data for fitting the model comes from tests on porcine adipose tissue [75] that offer a trove of data for modeling adipose tissue. The study in [75] contains several compressive stress-strain curves spanning decades of strain rates. A small sample of curves were extracted from their work and used for developing the adipose tissue in the model; these chosen stress-strain curves are shown in Fig. 30. As with some of the other materials, the high strain rates, i.e., those above  $1000/\text{s}$ , are accompanied by orders-of-magnitude increases in stress as compared to the lower strain rate data, but the increases for this material are much more extreme. As an example, an increase in strain rate from  $250/\text{s}$  to  $2100/\text{s}$  leads to the stress increasing from about  $4 \text{ kPa}$  to  $2500 \text{ kPa}$  at  $30$  percent strain, but this same massive increase is not observed when the strain rates increase from  $25/\text{s}$  to  $250/\text{s}$ . This nonlinearity makes adipose tissue a much more challenging material to model. However, Fig. 30 also shows that, relative to magnitudes, the stress behavior remains relatively consistent across all strain rates.

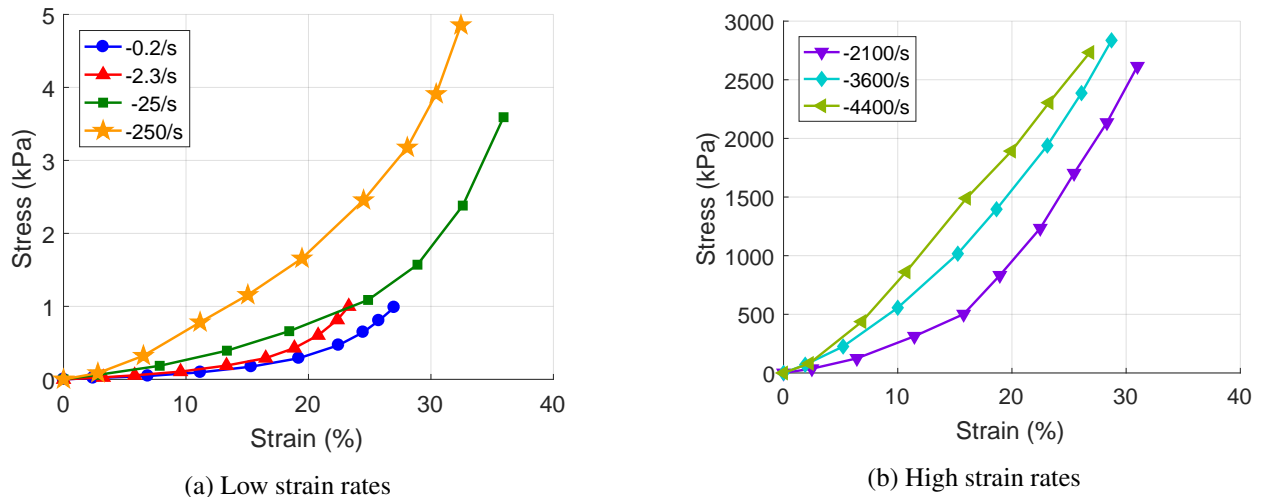


Fig. 30: Adipose tissue compressive stress-strain data for various strain rates (procine subject); experimental data originally presented in [75]

The model for adipose tissue consisted of a two-term Ogden model and two-term Prony series. Among the seven data sets shown in the Fig. 30, five were given non-zero weights in the chosen weight vector  $\mathbf{w} = [1, 1, 2, 4, 2, 0, 0]$  that corresponds to strain rates of  $-0.2/\text{s}$ ,  $-2.3/\text{s}$ ,  $-25/\text{s}$ ,  $-250/\text{s}$ ,  $-2100/\text{s}$ ,  $-3600/\text{s}$ , and  $-4400/\text{s}$ , respectively. The optimal parameter results from the global search are given in Table A4. Notably, the global search produced essentially the same estimate for both  $\alpha_i$  parameters (these parameters

differ in the thousandths place). This degree of similarity could potentially allow for the two terms to be combined, but, more importantly, the lack of uniqueness implies that two terms may not be necessary for the Ogden model.

The error for the optimization, as given in Table 5 is large but consistent with some of the more challenging materials to model. However, Fig. 31 reveals that this model could not capture both the low strain rate and high strain rate behavior. The model predictions for the lower strain rate data in Fig. 31a closely follow their respective experimental data curves, providing sound estimates. While the high strain rate data was only given modest weight during the optimization, the model demonstrated a complete inability to capture its behavior. This is not entirely surprising given the extreme (and nonlinear) increase in stress for the higher strain rates. It should be noted that a few different weighting schemes were attempted and additional optimization trials were conducted but none produced any better result; it is acknowledged that these additional trials were far from exhaustive, but they still considered several viable alternatives.

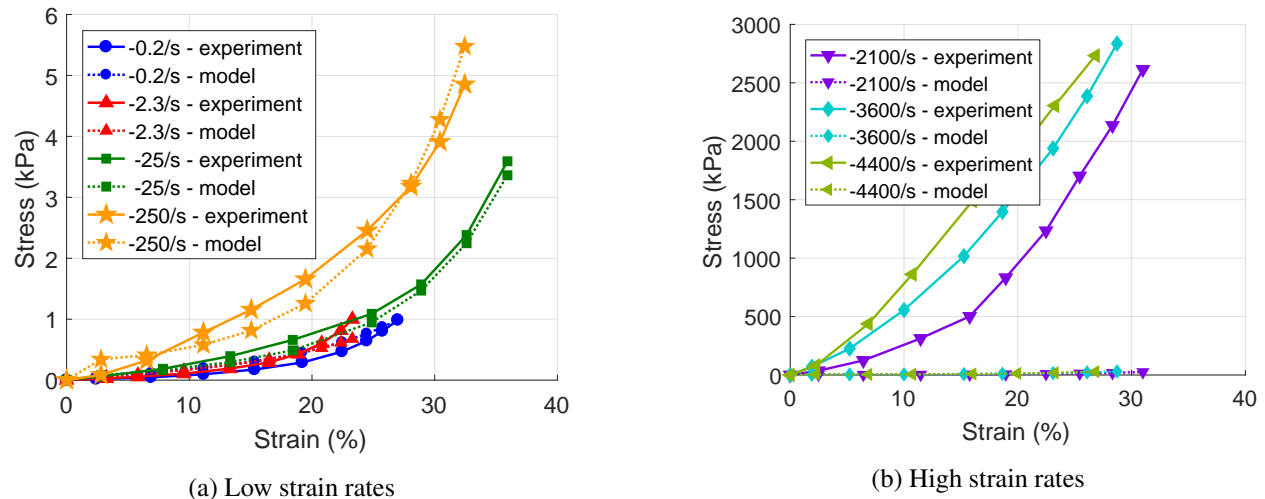


Fig. 31: Comparison of experimental stress-strain data and hyper-viscoelastic model for adipose tissue for various strain rates in compression (procine subject); experimental data originally presented in [75]

Plots of model-predicted stresses for assorted strain rates over strains ranging from  $-30$  percent to  $30$  percent are shown in Fig. 32. This figure demonstrates that an increase in strain rate from  $100/s$  to  $1000/s$  is accompanied by a substantial increase in stress, especially in tension, but these increases do not span enough orders of magnitude; this can be explained, however, by the lack of a nonlinear viscoelasticity in the model. This figure also exhibits the sharp transition between tension and compression around  $0$  percent strain, similar to that observed for the model of grey matter. Generally speaking, the model of the adipose tissue appears to be highly accurate and useful for strain rates ranging from  $0.1/s$  to  $250/s$  (and perhaps greater), but the insufficiency for strain rates at or above  $2000/s$  has been clearly demonstrated.

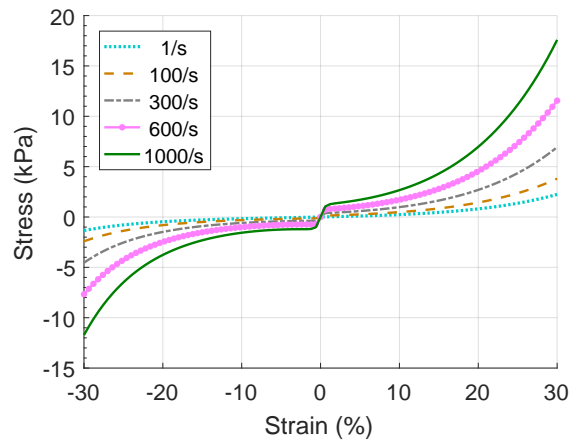


Fig. 32: Model-predicted stress for adipose tissue over a strain range of  $[-30\%, 30\%]$  for a variety of strain rates

Table 5: Final Cost Function Values for the Hyper-Viscoelastic Materials

Component	$\bar{O}$
Grey Matter	1.0554
White Matter	0.5216
Skin	1.9197
Heart	0.3968
Lungs	1.5646
Muscle	3.3177
Adipose	3.2977

#### 4. SUMMARY

This report details the steps taken to calibrate the material models incorporated into a computational model of a human head and the upper torso and head of a pig. A summary of some common constitutive model forms used to simulate the mechanical behavior of biological materials has been given, namely the  $U_s-U_p$  equation of state and hyperelastic, visco-elastic, and hyper-viscoelastic models. Additionally, uniaxial stress relationships have been derived for each model to easily relate constitutive model parameters to common experimental data forms. The optimization scheme employed for estimating the optimal constitutive model parameter values has been detailed. This optimization scheme minimizes the difference between uniaxial experimental data and model-predicted uniaxial stress.

The derived constitutive models and optimization method were implemented to calibrate parameters for each biological material identified in the greater model. The experimental data for each material was obtained from the available literature. Many of the models showed good agreement with their respective experimental data sets. Generally speaking, the models for the hyperelastic materials produced predictions that most closely approximated their respective experimental data. Bone was treated as the only purely viscoelastic material, and a single model calibration was used to find the appropriate model parameters. This was done because the generic model could be linearly scaled to match the different bone materials, e.g., cortical versus cancellous, present in the model. Some of the more challenging cases included those hyper-viscoelastic materials with separate data sets for tensile and compressive stress in which the behavior greatly differed between tension and compression, e.g., skin and muscle.

Many of the data sets utilized for this study represented a compromise as they possessed the necessary information to completely calibrate a constitutive model but avoided the difficulty that comes with combining or concatenating data from different sources. For instance, the calibration of a viscous material is better accomplished using dynamic material analysis, which is available for some biomaterials. However, large strain behavior is not captured by this test, and the superposition of two different tests further complicates the constitutive model calibration. Even the data chosen as a compromise is still not ideal, as many data sets are missing crucial decades of strain rate data, often in the range spanning 10/s to 100/s.

The hyper-viscoelastic materials were limited to models with a two-term Ogden series and two-term Prony series, but a more in-depth investigation should be conducted to determine the optimal number of terms for each material. In addition, the sensitivity of the different constitutive model parameters with respect to the model prediction error should also be a focus of future studies. The uncertainty associated with individual model parameters and their relationship to the larger uncertainty of the optimal model predictions must also be addressed. Another possible consideration for future work is the weight vectors applied to some of the larger data sets; these weights were chosen heuristically for the study, with preference given to those closest to expected strain rates for blast loading, but the impact of choosing different subsets of data and how those subsets are weighted should receive more consideration in the future. Further, only a single optimization method was presented here; however, many more exist, each with its own merits, and they should be investigated to determine if a particular scheme is better than that used here.

The purpose of this study is to provide a generalized framework for modeling biomaterials across many strain rates and data sources. In addition, the culmination of this study produced a set of comprehensive tables for computational modelers to quickly reference for future model development. However, this work is by no means a final product; rather, this work is a reflection of available data. It is intended for these material models to incorporate more data as it becomes available. Additionally, it is expected that future modelers will consider other data sets and strain rates that better reflect the threats, loading, or insults of primary concern to them. In this way, it is hoped that this report becomes both a template and starting point for future efforts in biomechanical modeling.

## ACKNOWLEDGMENTS

The authors are grateful for the technical discussions with and previous works performed by Nithyanand Kota, Shankarjee Krishnamoorthi, and Siddiq Qiddwai during their time at the Naval Research Laboratory (NRL). Funding for this project was provided by the Office of Naval Research (ONR) through the NRL Basic Research Program and by Tim Bentley at ONR.

## REFERENCES

1. T. L. Tanielian and L. H. Jaycox, "Invisible Wounds of War: Psychological and Cognitive Injuries, Their Consequences, and Services to Assist Recovery," Rept., RAND Corporation, Santa Monica, CA (2008).
2. F. P. DiMasi, R. H. Eppinger, and F. A. Bandak, "Computational Analysis of Head Impact Response Under Car Crash Loadings," Rept. No. 952718, SAE International, Warrendale, PA (1995).
3. E. G. Takhounts, R. H. Eppinger, J. Q. Campbell, R. E. Tannous, E. D. Power, and L. S. Shook, "On the Development of the SIMon Finite Element Head Model," *Stapp Car Crash Journal* **47**, 107–133 (2003).
4. E. G. Takhounts, S. A. Ridella, V. Hasija, R. E. Tannous, J. Q. Campbell, D. Malone, K. Danelson, J. Stitzel, S. Rowson, and S. Duma, "Investigation of Traumatic Brain Injuries Using the Next Generation of Simulated Injury Monitor (SIMon) Finite Element Head Model," *Stapp Car Crash Journal* **52**, 1–31 (2008).
5. L. Zhang, K. H. Yang, and A. I. King, "Comparison of Brain Responses Between Frontal and Lateral Impacts by Finite Element Modeling," *Journal of Neurotrauma* **18**(1), 21–30 (2001).
6. L. Zhang, K. H. Yang, and A. I. King, "A Proposed Injury Threshold for Mild Traumatic Brain Injury," *Journal of Biomechanical Engineering* **126**(2), 226–236 (2004).
7. H. Mao, L. Zhang, B. Jiang, V. V. Genthikatti, X. Jin, F. Zhu, R. Makwana, A. Gill, G. Jandir, A. Singh, and K. H. Yang, "Development of a Finite Element Human Head Model Partially Validated with Thirty Five Experimental Cases," *Journal of Biomechanical Engineering* **135**(11), 111002 (2013).
8. D. F. Moore, A. Jérusalem, M. Nyein, L. Noels, M. S. Jaffee, and R. A. Radovitzky, "Computational Biology — Modeling of Primary Blast Effects on the Central Nervous System," *NeuroImage* **47**(SUPPL. 2), T10–T20 (2009).
9. P. A. Taylor and C. C. Ford, "Simulation of Blast-Induced Early-Time Intracranial Wave Physics Leading to Traumatic Brain Injury," *Journal of Biomechanical Engineering* **131**(6), 061007 (2009).
10. J. Shridharani, G. Wood, M. Panzer, B. Capehart, M. Nyein, R. Radovitzky, and C. Bass, "Porcine Head Response to Blast," *Frontiers in Neurology* **3**(70), 1–12 (2012).
11. A. Säljö, F. Arrhén, H. Bolouri, M. Mayorga, and A. Hamberger, "Neuropathology and Pressure in the Pig Brain Resulting from Low-Impulse Noise Exposure," *Journal of Neurotrauma* **25**(12), 1397–1406 (2008).
12. M. Risling and J. Davidsson, "Experimental Animal Models for Studies on the Mechanisms of Blast-Induced Neurotrauma," *Frontiers in Neurology* **3**, 30 (2012).
13. R. A. Bauman, G. Ling, L. Tong, A. Januszkiwicz, D. Agoston, N. Delanerolle, Y. Kim, D. Ritzel, R. Bell, J. Ecklund, R. Armonda, F. Bandak, and S. Parks, "An Introductory Characterization of a Combat-Casualty-Care Relevant Swine Model of Closed Head Injury Resulting from Exposure to Explosive Blast," *Journal of Neurotrauma* **26**(6), 841–860 (2009).
14. F. Zhu, P. Skelton, C. C. Chou, H. Mao, K. H. Yang, and A. I. King, "Biomechanical Responses of a Pig Head Under Blast Loading: A Computational Simulation," *International Journal for Numerical Methods in Biomedical Engineering* **29**(3), 392–407 (2013).

15. J. A. Teland, F. Arrhén, A. Hamberger, M. Huseby, R. Rahimi, A. Säljö, and E. Svinsås, “Numerical Simulation of Mechanisms of Blast-Induced Traumatic Brain Injury,” *The Journal of the Acoustical Society of America* **127**(3), 1790 (2010).
16. R. K. Gupta and A. Przekwas, “Mathematical Models of Blast-Induced TBI: Current Status, Challenges, and Prospects,” *Frontiers in Neurology* **4**(59), 1–21 (2013).
17. T. El Sayed, A. Mota, F. Fraternali, and M. Ortiz, “A Variational Constitutive Model for Soft Biological Tissues,” *Journal of Biomechanics* **41**(7), 1458–1466 (2008).
18. T. El Sayed, A. Mota, F. Fraternali, and M. Ortiz, “Biomechanics of Traumatic Brain Injury,” *Computer Methods in Applied Mechanics and Engineering* **197**(51-52), 4692–4701 (2008).
19. S. Cheng, E. C. Clarke, and L. E. Bilston, “Rheological Properties of the Tissues of the Central Nervous System: A Review,” *Medical Engineering and Physics* **30**(10), 1318–1337 (2008).
20. P. G. Young, T. B. H. Beresford-West, S. R. L. Coward, B. Notarberardino, B. Walker, and A. Abdul-Aziz, “An Efficient Approach to Converting Three-Dimensional Image Data into Highly Accurate Computational Models,” *Philosophical Transactions of the Royal Society A: Mathematical, Physical and Engineering Sciences* **366**(1878), 3155 – 3173 (2008).
21. R. Said, J. Chang, P. Young, G. Tabor, and S. Coward, “Image-Based Meshing of Patient-Specific Data: Converting Medical Scans into Highly Accurate Computational Models,” in *2nd International Conference on Bioinformatics and Biomedical Engineering*, pp. 1672–1676, Shanghai, China (2008).
22. M. Otsuka, Y. Matsui, K. Murata, Y. Kato, and S. Itoh, “A Study on Shock Wave Propagation Process in the Smooth Blasting Technique,” *8th International LS-DYNA Users Conference* (2), 5–12 (2004).
23. M. S. Chafi, S. Ganpule, L. Gu, and N. Chandra, “Dynamic Response of Brain Subjected to Blast Loadings: Influence of Frequency Ranges,” *International Journal of Applied Mechanics* **03**(04), 803–823 (2011).
24. T. Rossi, B. Boccassini, L. Esposito, M. Iossa, A. Ruggiero, C. Tamburrelli, and N. Bonora, “The Pathogenesis of Retinal Damage in Blunt Eye Trauma: Finite Element Modeling,” *Investigative Ophthalmology and Visual Science* **52**(7), 3994–4002 (2011).
25. K. L. Monson, W. Goldsmith, N. M. Barbaro, and G. T. Manley, “Axial Mechanical Properties of Fresh Human Cerebral Blood Vessels,” *Journal of Biomechanical Engineering* **125**(2), 288–294 (2003).
26. T. C. Gasser, R. W. Ogden, and G. A. Holzapfel, “Hyperelastic Modelling of Arterial Layers with Distributed Collagen Fibre Orientations,” *Journal of the Royal Society Interface* **3**(6), 15–35 (2006).
27. X. Jin, K. H. Yang, and A. I. King, “Mechanical Properties of Bovine Pia-Arachnoid Complex in Shear,” *Journal of Biomechanics* **44**(3), 467–474 (2011).
28. L. Gu, M. S. Chafi, S. Ganpule, and N. Chandra, “The Influence of Heterogeneous Meninges on the Brain Mechanics Under Primary Blast Loading,” *Composites Part B: Engineering* **43**(8), 3160–3166 (2012).
29. A. N. Bashkatov, E. A. Genina, Y. P. Sinichkin, V. I. Kochubey, N. A. Lakodina, and V. V. Tuchin, “Glucose and Mannitol Diffusion in Human Dura Mater,” *Biophysical Journal* **85**(5), 3310–3318 (2003).

30. J. Ho and S. Kleiven, "Can Sulci Protect the Brain from Traumatic Injury?," *Journal of Biomechanics* **42**(13), 2074–2080 (2009).
31. G. Wollensak, E. Spoerl, and T. Seiler, "Stress-strain Measurements of Human and Porcine Corneas After Riboflavin-Ultraviolet-A-Induced Cross-Linking," *Journal of Cataract and Refractive Surgery* **29**(9), 1780–1785 (2003).
32. T. Mustafy, M. El-Rich, W. Mesfar, and K. Moglo, "Investigation of Impact Loading Rate Effects on the Ligamentous Cervical Spinal Load-Partitioning Using Finite Element Model of Functional Spinal Unit C2-C3," *Journal of Biomechanics* **47**(12), 2891–2903 (2014).
33. D. A. Zopf, C. L. Flanagan, H. B. Nasser, A. G. Mitsak, F. S. Huq, V. Rajendran, G. E. Green, and S. J. Hollister, "Biomechanical Evaluation of Human and Porcine Auricular Cartilage," *Laryngoscope* **125**(8), E262–E268 (2015).
34. J. Peterson and P. C. Dechow, "Material Properties of the Inner and Outer Cortical Tables of the Human Parietal Bone," *Anatomical Record* **268**(1), 7–15 (2002).
35. J. M. Alves, W. Xu, D. Lin, R. S. Siffert, J. T. Ryaby, J. J. Kaufman, and X. Wei, "Ultrasonic Assessment of Human and Bovine Trabecular Bone: A Comparison Study," *IEEE Transactions on Biomedical Engineering* **43**(3), 249–258 (1996).
36. C. Mercer, M. Y. He, R. Wang, and A. G. Evans, "Mechanisms Governing the Inelastic Deformation of Cortical Bone and Application to Trabecular Bone," *Acta Biomaterialia* **2**(1), 59–68 (2006).
37. C. L. Schwartz-Dabney and P. C. Dechow, "Variations in Cortical Material Properties Throughout the Human Dentate Mandible," *American Journal of Physical Anthropology* **120**(3), 252–277 (2003).
38. S. J. Kirkpatrick and B. W. Brooks, "Micromechanical Behaviour of Cortical Bone as Inferred from Laser Speckle Data," *Journal of Biomedical Materials Research* **39**, 373–9 (1998).
39. M. S. Chafi, G. Karami, and M. Ziejewski, "Biomechanical Assessment of Brain Dynamic Responses due to Blast Pressure Waves," *Annals of Biomedical Engineering* **38**(2), 490–504 (2010).
40. S. R. Ward and R. L. Lieber, "Density and Hydration of Fresh and Fixed Human Skeletal Muscle," *Journal of Biomechanics* **38**(11), 2317–2320 (2005).
41. T. Hachenberg, H. Lundquist, L. Tokics, B. Brismar, and G. Hedenstierna, "Analysis of Lung Density By Computed-Tomography Before and During General Anesthesia," *Acta Anaesthesiologica Scandinavica* **37**(6), 549–555 (1993).
42. A. Al-Mayah, J. Moseley, and K. K. Brock, "Contact Surface and Material Nonlinearity Modeling of Human Lungs," *Physics in Medicine and Biology* **53**(1), 305–317 (2008).
43. A. F. Bower, *Applied Mechanics of Solids* (CRC Press, Boca Raton, FL, 2010).
44. J. Simo and T. Hughes, *Computational Inelasticity* (Springer, New York, NY, 1998).
45. R. W. Ogden, "Large Deformation Isotropic Elasticity - On the Correlation of Theory and Experiment for Incompressible Rubberlike Solids," *Proceedings of the Royal Society of London. A. Mathematical and Physical Sciences* **326**(1567), 565–584 (1972).

46. O. H. Yeoh, "Some Forms of the Strain Energy Function for Rubber," *Rubber Chemistry and Technology* **66**(5), 754–771 (1993).
47. G. A. Holzapfel, T. C. Gasser, and R. W. Ogden, "A New Constitutive Framework for Arterial Wall Mechanics and a Comparative Study of Material Models," *Journal of Elasticity* **61**(1-3), 1–48 (2000).
48. MathWorks, "Matlab 2016b" (2016).
49. R. W. Ogden, G. Saccomandi, and I. Sgura, "Fitting hyperelastic models to experimental data," *Computational Mechanics* **34**(6), 484–502 (2004).
50. D. C. Drucker, "A Definition of Stable Inelastic Material," *Journal of Applied Mechanics* **26**(1), 101–106 (1959).
51. T. J. Horgan and M. D. Gilchrist, "Influence of FE Model Variability in Predicting Brain Motion and Intracranial Pressure Changes in Head Impact Simulations," *International Journal of Crashworthiness* **9**(4), 401–418 (2004).
52. Y. S. Shin, M. Lee, K. Y. Lam, and K. S. Yeo, "Modeling Mitigation Effects of Watershield on Shock Waves," *Shock and Vibration* **5**(4), 225–234 (1998).
53. D. J. Steinberg, "Spherical Explosions and the Equation of State of Water," Rept. No. UCID-20974, Lawrence Livermore National Laboratory, CA (1987).
54. K. Kuroda, "Forming of Al Alloy Plate by Underwater Shock Wave of Explosive," *6th European LS-DYNA Users Conference* (5), 127–136 (2007).
55. J. Kestin, M. Sokolov, and W. A. Wakeham, "Viscosity of Liquid Water in the Range 8 °C to 150 °C," *Journal of Physical and Chemical Reference Data* **7**(3), 941–948 (1978).
56. I. Bloomfield, I. Johnston, and L. Bilston, "Effects of Proteins, Blood Cells and Glucose on the Viscosity of Cerebrospinal Fluid," *Pediatric Neurosurgery* **28**(5), 246–251 (1998).
57. T. Rossi, B. Boccassini, L. Esposito, C. Clemente, M. Iossa, L. Placentino, and N. Bonora, "Primary Blast Injury to the Eye and Orbit: Finite Element Modeling," *Investigative Ophthalmology and Visual Science* **53**(13), 8057–8066 (2012).
58. X. Jin, J. B. Lee, L. Y. Leung, L. Zhang, K. H. Yang, and A. I. King, "Biomechanical Response of the Bovine Pia-Arachnoid Complex to Tensile Loading at Varying Strain-Rates," *Stapp Car Crash Journal* **50**, 637–649 (2006).
59. R. van Noort, M. M. Black, T. R. P. Martin, and S. Meanley, "A Study of the Uniaxial Mechanical Properties of Human Dura Mater Preserved in Glycerol," *Biomaterials* **2**(1), 41–45 (1981).
60. E. F. Morgan and T. M. Keaveny, "Dependence of Yield Strain of Human Trabecular Bone on Anatomic Site," *Journal of Biomechanics* **34**(5), 569–577 (2001).
61. J. C. M. Teo, K. M. Si-Hoe, J. E. L. Keh, and S. H. Teoh, "Relationship Between CT Intensity, Microarchitecture and Mechanical Properties of Porcine Vertebral Cancellous Bone," *Clinical Biomechanics* **21**(3), 235–244 (2006).
62. T. P. M. Johnson, S. Socrate, and M. C. Boyce, "A Viscoelastic, Viscoplastic Model of Cortical Bone Valid at Low and High Strain Rates," *Acta Biomaterialia* **6**(10), 4073–4080 (2010).



63. R. Eastell, L. Mosekilde, S. F. Hodgson, and B. L. Riggs, "Proportion of Human Vertebral Body Bone that Is Cancellous," *Journal of Bone and Mineral Research* **5**(12), 1237–1241 (1990).
64. S. L. Bonnick, *Bone Densitometry in Clinical Practice Applications and Interpretation*, 2nd ed. (Humana Press, Totowa, NJ, 2004).
65. D. F. Meaney, "Relationship Between Structural Modeling and Hyperelastic Material Behavior: Application to CNS White Matter," *Biomechanics and Modeling in Mechanobiology* **1**(4), 279–293 (2003).
66. F. Pervin and W. W. Chen, "Effect of Inter-Species, Gender, and Breeding on the Mechanical Behavior of Brain Tissue," *NeuroImage* **54**(SUPPL. 1), S98–S102 (2011).
67. B. A. Gama, S. L. Lopatnikov, and J. Gillespie John W, "Hopkinson Bar Experimental Technique: A Critical Review," *Applied Mechanics Reviews* **57**(4), 223–250 (2004).
68. O. A. Shergold, N. A. Fleck, and D. Radford, "The Uniaxial Stress Versus Strain Response of Pig Skin and Silicone Rubber at Low and High Strain Rates," *International Journal of Impact Engineering* **32**(9), 1384–1402 (2006).
69. J. Lim, J. Hong, W. W. Chen, and T. Weerasooriya, "Mechanical Response of Pig Skin Under Dynamic Tensile Loading," *International Journal of Impact Engineering* **38**(2-3), 130–135 (2011).
70. A. Anssari-Benam, D. L. Bader, and H. R. C. Screen, "A Combined Experimental and Modelling Approach to Aortic Valve Viscoelasticity in Tensile Deformation," *Journal of Materials Science: Materials in Medicine* **22**(2), 253–262 (2011).
71. Y. J. Zeng, D. Yager, and Y. C. Fung, "Measurement of the Mechanical Properties of the Human Lung Tissue," *Journal of Biomechanical Engineering* **109**(2), 169–174 (1987).
72. B. Sanborn, X. Nie, W. Chen, and T. Weerasooriya, "High Strain Rate Pure Shear and Axial Compressive Response of Porcine Lung Tissue," *Journal of Applied Mechanics* **80**(1), 1–6 (2013).
73. B. Song, W. Chen, Y. Ge, and T. Weerasooriya, "Dynamic and Quasi-Static Compressive Response of Porcine Muscle," *Journal of Biomechanics* **40**(13), 2999–3005 (2007).
74. X. Nie, J.-I. Cheng, W. W. Chen, and T. Weerasooriya, "Dynamic Tensile Response of Porcine Muscle," *Journal of Applied Mechanics* **78**(2), 021009 (2011).
75. K. Comley and N. Fleck, "The Compressive Response of Porcine Adipose Tissue from Low to High Strain Rate," *International Journal of Impact Engineering* **46**, 1–10 (2012).

## **Appendix A**

### **MATERIAL PROPERTIES AND MODEL PARAMETERS**

Table A1: Material Properties and Model Parameters for Components Modeled via Equations of State

Component	Constitutive Model	Material Properties and Model Parameters	Sources
Sinuses and Airway (Air)	Ideal gas equation of state (with viscosity)	$\rho = 1.1455 \text{ kg/m}^3$ $R = 287.058 \text{ J/(kg}\cdot^\circ\text{K)}$ $p_a = 101.325 \text{ kPa}$ $\zeta = 19.2 \times 10^{-6} \text{ Pa}\cdot\text{s}$	
CSF and Ventricles (CSF), and Venous Sinus and Bridging Vein Fluid (Blood)	$U_s-U_p$ equation of state	$\rho = 1000 \text{ kg/m}^3$ $c_0 = 1480 \text{ m/s}$ $s = 1.79$ $\Gamma_0 = 1.65$ $\zeta = 0.7 \text{ mPa}\cdot\text{s}$	[22, 23]
	Hyperelastic (neo-Hookean)	$C_{10} = 11.27 \text{ kPa}$ $D_1 = 9.13 \times 10^{-1} \text{ GPa}^{-1}$	[8]
Eyes (Vitreous)	$U_s-U_p$ equation of state	$\rho = 950 \text{ kg/m}^3$ $c_0 = 1450 \text{ m/s}$ $s = 1.79$ $\Gamma_0 = 1.65$ $\zeta = 5 \text{ Pa}\cdot\text{s}$	[22, 24]
	Hyperelastic (neo-Hookean)	$C_{10} = 3.8 \times 10^{-6} \text{ MPa}$ $D_1 = 1 \text{ GPa}^{-1}$	[57]

Table A2: Material Properties and Model Parameters for Components Treated as Hyperelastic Materials

Component	Constitutive Model	Material Properties and Model Parameters	Sources
Bridging Vein Walls	Anisotropic Hyperelastic (Holzapfel-Gasser-Ogden model)	$\rho = 1000 \text{ kg/m}^3$ $120 \text{ } \mu\text{m}$ thickness $c = 7.64 \text{ kPa}$ $k_1 = 996.6 \text{ kPa}$ $k_2 = 524.6$ $\kappa = 0.333$	[25, 26]
Pia Mater	Hyperelastic (2-term Ogden model)	$\rho = 1130 \text{ kg/m}^3$ $20 \text{ } \mu\text{m}$ thickness $\mu_1 = -6.41 \times 10^6, \mu_2 = 1.00 \times 10^7$ $\alpha_1 = -16.57, \alpha_2 = -24.29$	[27, 28]
Dura Mater	Hyperelastic (2-term Ogden model)	$\rho = 1130 \text{ kg/m}^3$ $550 \text{ } \mu\text{m}$ thickness $\mu_1 = -3.58 \times 10^6, \mu_2 = 4.57 \times 10^6$ $\alpha_1 = 11.84, \alpha_2 = 16.90$	[28, 29]
Falx and Tentorium	Hyperelastic (2-term Ogden model)	$\rho = 1130 \text{ kg/m}^3$ $\mu_1 = 9.77 \times 10^5, \mu_2 = 2.56 \times 10^5$ $\alpha_1 = 23.51, \alpha_2 = 23.22$	[30]
Sclera	Hyperelastic (2-term Ogden model)	$\rho = 1130 \text{ kg/m}^3$ $850 \text{ } \mu\text{m}$ thickness $\mu_1 = -1.27 \times 10^5, \mu_2 = 3.70 \times 10^5$ $\alpha_1 = 14.84, \alpha_2 = 16.53$	[28, 31]
Intervertebral Discs	Hyperelastic (Mooney-Rivlin model)	$\rho = 1200 \text{ kg/m}^3$ $C_{10} = 0.18 \text{ MPa}, C_{01} = 0.045 \text{ MPa}$ $\nu = 0.45$	[32]
Costal Cartilage	Hyperelastic (2-term Ogden model)	$\rho = 1240 \text{ kg/m}^3$ $\mu_1 = 8.05 \times 10^5, \mu_2 = -5.35 \times 10^5$ $\alpha_1 = -1.01, \alpha_2 = 3.65$	[8, 33]

Table A3: Material Properties and Model Parameters for Components Treated as Viscoelastic Materials

Component	Constitutive Model	Material Properties and Model Parameters	Sources
Cortical Skull Bone	Transversely Isotropic Viscoelastic	$\rho = 1841 \text{ kg/m}^3$ $E_3 = 11.8 \text{ GPa}; E_1, E_2 = 16.65 \text{ GPa}$ $G_{12} = 6.4 \text{ GPa}; G_{13}, G_{23} = 4.25 \text{ GPa}$ $\nu_{12} = 0.30; \nu_{13}, \nu_{23} = 0.3975; \nu_{31}, \nu_{32} = 0.32$	[34]
Cancellous Skull Bone	Transversely Isotropic Viscoelastic	$\rho = 100 \text{ kg/m}^3$ $E_3 = 375 \text{ MPa}; E_1, E_2 = 530 \text{ MPa}$ $G_{12} = 204 \text{ MPa}; G_{13}, G_{23} = 135 \text{ MPa}$ $\nu_{12} = 0.30; \nu_{13}, \nu_{23} = 0.3975; \nu_{31}, \nu_{32} = 0.32$	[35, 36]
Vertebrae	Viscoelastic	$\rho = 485.4 \text{ kg/m}^3$ $E = 3273 \text{ MPa}$ $\nu = 0.30$	[32]
Ribs	Viscoelastic	$\rho = 1841 \text{ kg/m}^3$ $E = 9 \text{ GPa}$ $\nu = 0.30$	[34, 38]
Sternum	Viscoelastic	$\rho = 485.4 \text{ kg/m}^3$ $E = 3273 \text{ MPa}$ $\nu = 0.30$	[32]
Cortical Bone Model <sup>a</sup>	2-term Prony series	$E = 20.2 \text{ GPa}$ $\nu = 0.30$ $g_1 = 0.4838, g_2 = 0.1336$ $\tau_1 = 1.32 \times 10^{-5}, \tau_2 = 6.00 \times 10^{-2}$	[62]
Mandible	Transversely Isotropic Viscoelastic (2-term Prony series)	$\rho = 1925 \text{ kg/m}^3$ $E_3 = 12.7 \text{ GPa}; E_1, E_2 = 20.35 \text{ GPa}$ $G_{12} = 7.4 \text{ GPa}; G_{13}, G_{23} = 5.25 \text{ GPa}$ $\nu_{12} = 0.375; \nu_{13}, \nu_{23} = 0.39; \nu_{31}, \nu_{32} = 0.245$ $g_1 = 0.1336, g_2 = 0.4838$ $\tau_1 = 6.00 \times 10^{-2}, \tau_2 = 1.32 \times 10^{-5}$	[37]

<sup>a</sup> These model parameters were used for all viscoelastic bone materials, except for the mandible, with the ratio of elastic moduli ( $E_{\text{material}}/E_{\text{model}}$ ) used for scaling.

Table A4: Material Properties and Model Parameters for Components Treated as Hyper-viscoelastic Materials

Component	Constitutive Model	Material Properties and Model Parameters	Sources
Grey Matter – Cerebrum and Cerebellum	Hyper-viscoelastic (2-term Ogden, 2-term Prony)	$\rho = 1040 \text{ kg/m}^3$ $\mu_1 = 6.74 \times 10^3, \alpha_1 = 10.18, \mu_2 = 9.08 \times 10^6, \alpha_2 = 2.74$ $g_1 = 0.0019, \tau_1 = 1.79 \times 10^{-1}, g_2 = 0.9980, \tau_2 = 3.14 \times 10^{-7}$	[8]
White Matter – Cerebrum and Cerebellum, Brain Stem, Spinal Cord, Optic Nerves	Hyper-viscoelastic (2-term Ogden, 2-term Prony)	$\rho = 1040 \text{ kg/m}^3$ $\mu_1 = 6.90 \times 10^5, \alpha_1 = 4.13, \mu_2 = -9.47 \times 10^4, \alpha_2 = 6.37$ $g_1 = 0.8070, \tau_1 = 2.40 \times 10^{-5}, g_2 = 0.1861, \tau_2 = 1.31 \times 10^{-7}$	[8]
Skin	Hyper-viscoelastic (2-term Ogden, 2-term Prony)	$\rho = 1200 \text{ kg/m}^3$ $K_0 = 34.7 \text{ MPa}$ $\mu_1 = 1.11 \times 10^6, \alpha_1 = -11.59, \mu_2 = 4.48 \times 10^5, \alpha_2 = 11.38$ $g_1 = 0.8453, \tau_1 = 1.54 \times 10^{-6}, g_2 = 0.1421, \tau_2 = 1.70 \times 10^{-3}$	[8, 39]
Heart	Hyper-viscoelastic (2-term Ogden, 2-term Prony)	$\rho = 1060 \text{ kg/m}^3$ $K_0 = 3.33 \text{ MPa}$ $\mu_1 = 4.15 \times 10^6, \alpha_1 = 15.58, \mu_2 = 3.85 \times 10^6, \alpha_2 = 11.51$ $g_1 = 0.2209, \tau_1 = 5.99 \times 10^0, g_2 = 0.7537, \tau_2 = 3.22 \times 10^{-10}$	[8, 40]
Lungs	Hyper-viscoelastic (2-term Ogden, 2-term Prony)	$\rho = 235 \text{ kg/m}^3$ $\nu = 0.43$ $\mu_1 = -8.95 \times 10^5, \alpha_1 = -1.32, \mu_2 = 2.11 \times 10^6, \alpha_2 = 2.41$ $g_1 = 0.5802, \tau_1 = 1.14 \times 10^{-7}, g_2 = 0.4187, \tau_2 = 6.07 \times 10^{-6}$	[41, 42]
Muscle	Hyper-viscoelastic (2-term Ogden, 2-term Prony)	$\rho = 1060 \text{ kg/m}^3$ $\kappa_0 = 3.33 \text{ MPa}$ $\mu_1 = -1.36 \times 10^6, \alpha_1 = -0.84, \mu_2 = 2.49 \times 10^6, \alpha_2 = 3.36$ $g_1 = 0.5312, \tau_1 = 4.21 \times 10^{-5}, g_2 = 0.4298, \tau_2 = 7.95 \times 10^{-6}$	[8, 40]
Adipose Tissue	Hyper-viscoelastic (2-term Ogden, 2-term Prony)	$\rho = 1200 \text{ kg/m}^3$ $K_0 = 34.7 \text{ MPa}$ $\mu_1 = 3.79 \times 10^5, \alpha_1 = 13.53, \mu_2 = 2.68 \times 10^5, \alpha_2 = 13.53$ $g_1 = 0.8141, \tau_1 = 2.77 \times 10^{-12}, g_2 = 0.1851, \tau_2 = 3.45 \times 10^{-6}$	[8, 39]